

Boundary-layer structures arising in linear transport theoryE. L. Gaggioli ^{1,2,3,*}, Laura C. Estrada ^{1,2,†} and Oscar P. Bruno ^{3,‡}¹*Universidad de Buenos Aires, Facultad de Ciencias Exactas y Naturales, Departamento de Física, Buenos Aires 1428, Argentina*²*CONICET–Universidad de Buenos Aires, Instituto de Física de Buenos Aires (IFIBA), Buenos Aires 1428, Argentina*³*Department of Computing and Mathematical Sciences, Caltech, Pasadena, California 91125, USA*

(Received 26 March 2024; accepted 17 July 2024; published 28 August 2024)

We consider boundary-layer structures that arise in connection with the transport of neutral particles (e.g., photons or neutrons) through a participating medium. Such boundary-layer structures were previously identified by the authors in certain particular cases [Phys. Rev. E **104**, L032801 (2021)]. Extending the previous work to anisotropic scattering and general Fresnel boundary conditions, this contribution presents computational algorithms which (1) resolve the aforementioned layers as well as previously unreported boundary layers associated with Fresnel boundary transmission and reflection, and (2) yield accurate simulations at fixed computational cost for transport under phase functions with arbitrarily strong anisotropy. The present paper additionally includes (3) Mathematical proofs which justify the numerical methods proposed for resolution of boundary-layer structures. The impact of the new theory on algorithmic performance is demonstrated through a series of 1D computational benchmarks that emulate typical photon- and neutron-transport applications such as, e.g., optical tomography, and nuclear reactor analysis and design. Experimental results for transmission of photons through turbid media are presented, exhibiting close agreement between simulated and experimental data. As illustrated by means of a variety of numerical results, the proposed boundary-layer-based approach tackles transport problems with unprecedented accuracy and efficiency.

DOI: [10.1103/PhysRevE.110.025306](https://doi.org/10.1103/PhysRevE.110.025306)**I. INTRODUCTION**

We are concerned with the problem of transport of neutral particles such as neutrons [1,2] and photons [3,4], wherein interactions between particles are negligible and only interactions between the particles and a background medium need to be taken into account. The transport processes considered, in which the background medium may absorb, emit, and/or scatter neutral particles, is governed by the linear single-species version of the Boltzmann equation, namely, the linear transport equation—which is alternatively known as the radiative transfer equation (RTE) and the neutron-transport equation in the contexts of photon and neutron transport [5,6], respectively. The linear transport equation presents the challenge of high dimensionality: in full three-dimensional (3D) space the solution (particle density) depends on three spatial variables as well as two angular propagation variables and time, giving rise, in all, to a computationally demanding six-dimensional problem. Important applications include radiative heat transport [7,8], gas dynamics [2], radiation transport in stellar and planetary atmospheres [3,9,10], cancer diagnosis [11–13], radiation therapy dose planning [14], finger joint arthritis diagnosis [15,16], studies of the human brain function [17,18], optical and fluorescence tomography [19–21], and neutron transport for nuclear reactor design [22–24], among others [25–27].

This paper presents numerical algorithms that enable effective treatment of certain boundary-layer structures arising in the solutions of the linear transport equation which were previously identified in Ref. [28] under the assumptions of vacuum boundary conditions and isotropic scattering. As noted in Ref. [28], if left unaddressed, the presence of unbounded derivatives in the boundary-layer regions poses a significant challenge for the numerical solution of transport equations. Expanding on the previous work, which, in particular, provides a means for accurate and inexpensive numerical treatment of boundary layers, the methods introduced in the present paper enable treatment of problems under strongly anisotropic scattering (on the basis of a certain multiresolution approach for the evaluation of the scattering integral), and they can be applied under general Fresnel boundary conditions (which, as shown in Sec. III A and throughout this paper, themselves give rise to a different type of boundary-layer structure). The proposed methods for regularization of both types of boundary layers are based on the use of certain regularizing changes of variables under which unbounded derivatives are eliminated. These methods, which are presented here in a spatially one-dimensional (1D) context, are directly applicable to fully 3D configurations. This paper additionally includes (1) a mathematical analysis of the regularization process and associated algorithms, providing a firm mathematical basis for the proposed methods and (2) comparisons with experimental results for turbid media exhibiting close agreement between experiments and numerical simulations.

The linear-transport boundary layers identified in Ref. [28], whose theoretical description and numerical resolution via

*Contact author: egaggioli@df.uba.ar†Contact author: lestrada@df.uba.ar‡Contact author: obruno@caltech.edu

changes of variables are detailed and generalized in the present paper, are inherent in the transport equation solutions near boundaries, and by extension, to the solutions of Boltzmann-type equations. These boundary layers are unrelated to the ones widely discussed in the literature over a period of various decades [29–33], which concern the asymptotic diffusion limit of the transport equation, that is, equations of the form of Eqs. (1) or (3) in the limit of large scattering coefficient μ_s proportional to ε^{-1} and small absorption $\mu_a = \mu_t - \mu_s$, proportional to ε , where ε is a small parameter. The boundary layers that arise in the resulting diffusion approximation are independent of the angular variable ξ . In contrast, the boundary layers considered in this paper exist for arbitrary scattering and absorption coefficients, and they are only observed for small values of ξ (directions nearly parallel to the boundary) and for directions near the critical direction $\xi = \xi_c^0$ of total internal reflection.

The remainder of this paper is organized as follows. Section II briefly sets up necessary notations and conventions. Section III then develops the boundary-layer theory for the linear transport equation and it presents mathematical proofs showing that all associated boundary-layer structures can be completely resolved by means of certain types of changes of variables in the spatial and angular coordinates. Section IV present numerical techniques based on the theoretical background provided by the previous sections as well as a multiresolution algorithm tailored to handle effectively the scattering integral under highly anisotropic phase functions. Numerical and experimental results are then presented in Sec. V, highlighting the efficiency and accuracy of the proposed algorithms, and including applications to configurations involving collimated sources (such as those necessary for modeling laser beams), as well as an experimental illustration demonstrating excellent agreement between theory and experiment. Finally, Sec. VI presents a few concluding remarks and it outlines future research directions emerging from the present work, including, in particular, the introduction of enhanced imaging techniques based on joint inversion of fluorescence-microscopy and diffuse optical-tomography data, as suggested in Ref. [34], with the goal of overcoming some of the inherent limitations of the fluorescence-microscopy technique in high-scattering media.

II. BACKGROUND

For simplicity and definiteness this paper focuses on 1D configurations (Fig. 1) governed by the scalar radiative transfer equation. The radiative transfer model is applicable to propagation of monoenergetic particles, including neutron transport [5] as well as photon transport under unpolarized radiation as is often found in the context of light propagation in highly scattering media such as biological tissue [15,16,21,32]; discussions concerning the possible existence of polarization effects can be found in Refs. [35,36]. The more general vector radiative transfer equation that accounts for multiple polarization states [4,37], however, can be treated similarly (cf. Remark 1). Both time dependent and steady state configurations are considered in the results and discussion section, but for definiteness, the boundary-layer analysis is presented in the steady state context only. (A corresponding

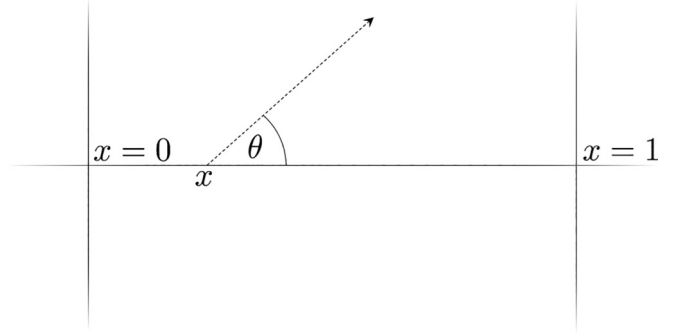


FIG. 1. 1D finite “slab” geometry (from Ref. [28]): $\xi = \cos(\theta)$.

analysis for the time-dependent case, which can be treated by means of similar techniques, is left for future work.) The analysis given below can also be extended to the general multidimensional case, for which the 1D configuration might be considered as a limiting case near the domain boundary.

The 1D linear transport problem

$$\begin{aligned} \xi \frac{\partial}{\partial x} u(x, \xi) + \mu_t(x) u(x, \xi) \\ = \mu_s(x) \Phi(x, \xi) + q(x, \xi), \end{aligned}$$

$$u(0, \xi) = \ell_0(\xi) + \mathcal{R}^0(\xi) u(0, \xi_R), \quad \text{for } \xi > 0,$$

$$u(1, \xi) = \ell_1(\xi) + \mathcal{R}^1(\xi) u(1, \xi_R), \quad \text{for } \xi < 0, \quad (1)$$

where

$$\Phi(x, \xi) = \int_{-1}^1 p(\xi, \xi') u(x, \xi') d\xi', \quad (2)$$

describes the dynamics of the angular flux $u(x, \xi)$, where $x, \xi' = \cos(\theta')$ and $\xi = \cos(\theta)$ denote the spatial variable and the cosines of the relevant propagation angles, as depicted in Fig. 1, respectively. Here, calling $\mu_a(x)$ and $\mu_s(x)$ the absorption and scattering coefficients, $\mu_t(x) = \mu_s(x) + \mu_a(x)$ denotes the total transport coefficient. The phase function $p(\xi, \xi')$ models the density of probability that particles incident at x in directions between ξ' and $\xi' + d\xi'$ emerge from x in the direction ξ after a scattering event. The “volumetric source” q models the emission of particles, such as photons or neutrons, within the medium, as a result of, e.g., fluorescence or nuclear fission. The terms $\ell_i(\xi)$ ($i = 0, 1$) can be used to model a source of photons at the domain boundaries, as may be given by a laser beam that injects radiation for optical tomography applications, and finally, $\mathcal{R}^{0,1}$ denote the Fresnel coefficients which, as discussed below in this section, themselves give rise to boundary-layer structures whose adequate resolution impacts significantly on the accuracy of the numerical solution of the transport equation.

The corresponding time-dependent problem,

$$\begin{aligned} \left[\frac{1}{c} \frac{\partial}{\partial t} + \xi \frac{\partial}{\partial x} + \mu_t(x) \right] u(x, \xi, t) \\ = \mu_s(x) \Phi(x, \xi, t) + q(x, \xi, t), \quad u(x, \xi, t = 0) = 0, \end{aligned}$$

$$u(0, \xi, t) = \ell_0(\xi, t) + \mathcal{R}^0(\xi)u(0, \xi_R, t), \quad \text{for } \xi > 0,$$

$$u(1, \xi, t) = \ell_1(\xi, t) + \mathcal{R}^1(\xi)u(1, \xi_R, t), \quad \text{for } \xi < 0, \quad (3)$$

where

$$\Phi(x, \xi, t) = \int_{-1}^1 p(\xi, \xi')u(x, \xi', t)d\xi' \quad (4)$$

and where c denotes the speed of the particles in the participating media (which is taken to equal $c = 1$ throughout this paper), incorporates a time derivative in the differential equation as well as the prescription of the values of the solution at the initial time and time-dependent boundary conditions, in addition to various elements present in Eq. (1).

The previous contribution [28] announced results concerning boundary-layer structures for the transport equations in the presence of so-called vacuum boundary conditions—that is, $u(x, \xi) = 0$ at $x = 0$ and $x = 1$ for the relevant ranges of incoming directions, namely $0 < \xi \leq 1$ for $x = 0$ and $-1 \leq \xi < 0$ for $x = 1$. [Clearly, the vacuum boundary conditions coincide with Fresnel boundary conditions, displayed in Eqs. (1) and (3), with $\mathcal{R}^{0,1} = 0$ and $\ell_{0,1} = 0$.] Photon transport theories (as, e.g., required for applications in optical tomography) generally require the use of the Fresnel boundary conditions with nonzero Fresnel coefficients. The Fresnel coefficient, which depends on the indexes of refraction n_Ω and n_s of the participating medium and its surroundings (both of which are assumed throughout this paper to be spatially constant for simplicity), quantifies the fraction of the radiation arriving at the boundary in a given direction, that is reflected in the corresponding specular direction. For the 1D slab geometry considered in this paper, radiation incident on the boundary in the direction $\xi = \cos(\theta)$ is specularly reflected into direction $\xi_R = -\xi$. Calling $\alpha^0 = \pi - \theta$ the incidence angle with respect to the normal $\hat{v}^0 = (1, 0, 0)$ at $x = 0$ and $\alpha^1 = \theta$ the incidence angle with respect to the normal $\hat{v}^1 = (-1, 0, 0)$ at $x = 1$, and letting $\alpha^{0,1}$ denote either α^0 or α^1 depending on whether the normal at \hat{v}^0 at $x = 0$ or \hat{v}^1 at $x = 1$ is considered, the corresponding Fresnel coefficient $\mathcal{R}^{0,1}$ (similarly equal to

either \mathcal{R}^0 or \mathcal{R}^1) is given by

$$\mathcal{R}^{0,1}(\xi) = \begin{cases} \left(\frac{n_\Omega - n_s}{n_\Omega + n_s}\right)^2 & \text{if } \alpha^{0,1} = 0, \\ \frac{1}{2} \left(\frac{\sin^2(\alpha_t^{0,1} - \alpha^{0,1})}{\sin^2(\alpha_t^{0,1} + \alpha^{0,1})} + \frac{\tan^2(\alpha_t^{0,1} - \alpha^{0,1})}{\tan^2(\alpha_t^{0,1} + \alpha^{0,1})} \right) & \text{if } 0 < \alpha^{0,1} < \alpha_c^{0,1}, \\ 1 & \text{if } \alpha^{0,1} \geq \alpha_c^{0,1}, \end{cases} \quad (5)$$

where the critical angle is given by $\sin(\alpha_c^{0,1}) = \frac{n_s}{n_\Omega}$, with associated critical directions

$$\xi_c^0 = \cos(\alpha_c^0) \quad \text{and} \quad \xi_c^1 = \cos(\alpha_c^1) \quad (6)$$

(beyond which, for $n_\Omega > n_s$, total internal reflection occurs at the boundaries $x = 0$ and $x = 1$, respectively). Note that, under the present assumptions of a constant index of refraction we have

$$\xi_c^1 = -\xi_c^0. \quad (7)$$

The transmission angles $\alpha_t^{0,1}$ are obtained from Snell's law of refraction $\sin(\alpha_t^{0,1}) = \frac{n_\Omega}{n_s} \sin(\alpha^{0,1})$.

On the basis of the Fresnel coefficient we additionally define the measurement operator

$$\mathcal{J}^+[u](t) = \int_0^1 [1 - \mathcal{R}^1(\xi)]u(1, \xi, t)d\xi, \quad (8)$$

which quantifies the time-resolved outgoing flux of photons at the boundary domain at $x = 1$.

III. BOUNDARY-LAYER THEORY FOR THE LINEAR TRANSPORT EQUATION

A. Integral equation formulation: Fresnel and incidence boundary layers

An integral equation equivalent to Eq. (1) can readily be obtained by utilizing an integrating factor and substituting the $x = 0$ and $x = 1$ boundary conditions (1) in the resulting equation. For $\xi > 0$ we thus obtain

$$u(x, \xi) = (\ell_0(\xi) + \mathcal{R}^0(\xi)u(0, \xi_R))e^{-\int_0^x \mu_t(y)dy/\xi} + \frac{e^{-\int_0^x \mu_t(y)dy/\xi}}{\xi} \int_0^x e^{\int_0^y \mu_t(z)dz/\xi} q(y, \xi)dy$$

$$+ \frac{e^{-\int_0^x \mu_t(y)dy/\xi}}{\xi} \int_0^x e^{\int_0^y \mu_t(z)dz/\xi} \mu_s(y) \int_{-1}^1 p(\xi, \xi')u(y, \xi')d\xi'dy, \quad \xi > 0, \quad (9)$$

with a similar expression for $\xi < 0$. In view of the ideas underlying boundary-layer theory [38], the particular case of Eq. (9) in which the quantities μ_s , μ_t , and q are spatially constant captures the leading order boundary-layer behavior [28] of the solution u of the variable-coefficients problem—since, for a lowest-order asymptotic approximation $u_0(x, \xi)$, where $u(x, \xi) \sim u_0(x, \xi)$ as $(x, \xi) \rightarrow (0^+, 0^+)$, the coefficients can indeed be assumed to be constant in a small neighborhood of the boundary points. Assuming such constant coefficients and using Eqs. (2) and (9) leads to the near-boundary approximation

$$u(x, \xi) \sim u_0(x, \xi) = (\ell_0(\xi) + \mathcal{R}^0(\xi)u(0, \xi_R))e^{-\mu_t(0)x/\xi} + \frac{e^{-\mu_t(0)x/\xi}}{\xi} \int_0^x e^{\mu_t(0)y/\xi} q(0, \xi)dy$$

$$+ \frac{e^{-\mu_t(0)x/\xi}}{\xi} \int_0^x e^{\mu_t(0)y/\xi} \mu_s(0)\Phi(y, \xi)dy, \quad \text{as } (x, \xi) \rightarrow (0^+, 0^+), \quad (10)$$

with a similar result for $(x, \xi) \rightarrow (1^-, 0^-)$. The exponential factor $\exp(-\mu_t(0)x/\xi)$ represent fast transitions in the density of particles traveling near the boundary point $x = 0$ in directions nearly parallel to the boundary (for which ξ is close to zero). In particular, these exponential boundary-layer terms entail unbounded derivatives in both, the x and ξ variables as $(x, \xi) \rightarrow (0^+, 0^+)$. Clearly, such boundary layers present a challenge from a computational standpoint—since the numerical solution of Eq. (1) requires, in particular, x differentiation and integration respect to ξ across such structures.

The boundary-layer terms $\ell_0(\xi)e^{-\int_0^x \mu_t(y)dy/\xi}$ in Eq. (9) and $\ell_0(\xi)e^{-\mu_t(0)x/\xi}$ in Eq. (10) represent the uncollided and unabsorbed remainder of the incident flux entering through the domain boundary $x = 0$; these terms are therefore called “incidence boundary layers” (IBL). Similarly, the third and fourth boundary-layer terms in Eqs. (9) and (10) incorporate exponential increments and attenuations—arising from the emission of particles resulting from the volumetric source q in the third terms, and from particle scattering Φ in the fourth terms, and they are therefore called “volumetric source boundary layers” (VSBL). The terms $\mathcal{R}^0(\xi)u(0, \xi_R)e^{-\int_0^x \mu_t(y)dy/\xi}$ and $\mathcal{R}^0(\xi)u(0, \xi_R)e^{-\mu_t(0)x/\xi}$ in these equations, finally, represent the uncollided and unabsorbed remainders of Fresnel reflections of interior fields at the boundary $x = 0$, and they incorporate boundary layers of a different kind, which we call “Fresnel boundary layers” (FBL). Unlike the IBL and VSBL, the Fresnel boundary layers around, e.g., $x = 0$ arises from a singularity of the Fresnel reflection coefficient $\mathcal{R}^0(\xi)$ at the boundary ξ_c^0 between the angular regimes of partial and total internal reflection, as discussed in what follows. Notably, unlike the IBL and VSBL, the Fresnel boundary layers induce a singular behavior throughout the spatial domain, and, strictly speaking, they are not confined to the domain boundary. However, owing to the exponential factor that accompanies the Fresnel coefficients, such singularities decay exponentially fast with the distance to the boundary, they are therefore only observed in a neighborhood of the boundary (see, e.g., Fig. 7), and, in that sense, they are boundary layers as well.

As mentioned above, the FBL arise as ξ approaches the total internal-reflection direction ξ_c^0 from the right (respectively, ξ_c^1 from the left). At such points all derivatives of $\mathcal{R}^{0,1}(\xi)$ become infinite, which gives rise to fast transitions in the solution u around the points $(x, \xi) = (0, \xi_c^0)$ and $(x, \xi) = (1, \xi_c^1)$, as illustrated in the aforementioned Fig. 7. To see this for $\mathcal{R}^0(\xi)$ (the case $\mathcal{R}^1(\xi)$ is analogous) we note a singularity that arises in this function from the term

$$\alpha_t^0 = \arcsin\left(\frac{n_\Omega}{n_s}\sqrt{1-\xi^2}\right) \quad (11)$$

that appears repeatedly in Eq. (5). Expanding $\frac{n_\Omega}{n_s}\sqrt{1-\xi^2}$ around $\xi = \xi_c^0$ (for which $\frac{n_\Omega}{n_s}\sqrt{1-(\xi_c^0)^2} = 1$) we obtain $\frac{n_\Omega}{n_s}\sqrt{1-\xi^2} \sim 1 + \frac{n_\Omega^2}{n_s^2}\xi_c^0(\xi - \xi_c^0)$ which, together with Eq. (11) and $\arcsin(y) \sim \frac{\pi}{2} - \sqrt{2}\sqrt{1-y}$ for $y \lesssim 1$ yields

$$\alpha_t^0 \sim \frac{\pi}{2} - \frac{n_\Omega}{n_s}\sqrt{2\xi_c^0}\sqrt{\xi - \xi_c^0}, \quad (12)$$

or, more precisely,

$$\alpha_t^0 = F\left(\sqrt{\xi - \xi_c^0}\right), \quad \xi > \xi_c^0, \quad (13)$$

where $F = F(z)$ is a smooth function of z around $z = 0$. These expressions encapsulate the singular character

$$\mathcal{R}^0(\xi) = 1 - a\sqrt{\xi - \xi_c^0} + \mathcal{O}(\xi - \xi_c^0), \quad (14)$$

for some real coefficient $a > 0$, or, more generally,

$$\mathcal{R}^{0,1}(\xi) = S^{0,1}\left(|\xi - \xi_c^{0,1}|^{\frac{1}{2}}\right), \quad (15)$$

of the complete Fresnel coefficient and its unbounded derivatives for $\xi \geq \xi_c^0$ and $\xi \leq \xi_c^1$, where $S^{0,1} = S^{0,1}(z)$ is a smooth function of z around $z = 0$. As indicated above, the exponentially decaying factors that accompany the Fresnel coefficients make the fast FBL transitions observable only in a small region near the boundary points, as befits a boundary-layer structure.

Remark 1. As suggested in Sec. II, with exception of minor variations required to account for the simultaneous presence of multiple polarization states, the theoretical and computational methods presented in this paper are applicable in the context of vector radiative transfer equations for polarized light. In particular, since Snell’s law (11) is valid for arbitrary polarization states, the singular character of the Fresnel reflection matrix [37, Eq. (10)] is once again, as in Eqs. (13) and (15), given by smooth functions of $|\xi - \xi_c^{0,1}|^{\frac{1}{2}}$ for $\xi \geq \xi_c^0$ and $\xi \leq \xi_c^1$. It follows that the change of variables (18), which was designed to regularize functions containing such types of singularities, also produces the required regularization for the Fresnel reflection matrices and associated vector-transport solutions that arise under polarized radiation.

B. Boundary-layer resolving changes of variables

As discussed in what follows, certain angular and spatial changes of variables can be utilized to fully resolve numerically the near-singular IBL, VSBL, and FBL structures described in the previous section; such a result was previously announced for the VSBL structures in Ref. [28]. The theoretical results presented in Secs. III C and III D, which are illustrated in Fig. 6, show that, indeed, such transformations “regularize” the problem: in the new variables the spatial and angular derivatives remain uniformly bounded throughout the spatial and angular domains, including points in space arbitrarily close to the domain boundary and directions arbitrarily close to tangential to the boundary. As a result, use of the new variables gives rise to rapidly convergent numerical algorithms that, on the basis of relatively coarse discretizations, evaluate accurately the transport solution throughout the angular and spatial domains, and, in particular, for arbitrarily small values of ξ and for values of x arbitrarily close to the boundaries $x = 0$ and $x = 1$.

As a simple example, let us consider the function $w(\xi) = \sqrt{\xi}$ which, like the Fresnel coefficient, has infinite derivatives at a point—in this case, the point $\xi = 0$. Clearly, use of the change of variables $\xi = r^n$ with an integer $n > 1$ in an integration problem results in the smoother integrand $nw(r^n)r^{n-1} = nr^{3n/2-1}$ —which, of course, is infinitely differentiable for n

even, and, in particular, for $n = 2$. Note that an equispaced mesh in the r variable corresponds to a graded mesh in the ξ variable: the mesh grading transforms a curve with an infinite slope in the ξ variable into a curve with a finite slope in the r variable—a property that will be exploited not only in connection with the Fresnel boundary layers, but also, with values $n > 2$, to resolve the challenging nearly singular ξ dependence of the aforementioned IBL and VSBL.

As shown in Secs. III C and III D, changes of variables can similarly be utilized to resolve the unbounded x derivatives that occur in a family of functions such as $w(x, \xi) = 1 - e^{-\frac{x}{\xi}}$. Whereas none of these functions has an infinite derivative, the derivatives of the family of functions are collectively unbounded, as, e.g., the x -derivatives of $w_\xi(x)$ (e.g., the first derivative $w'_\xi(x) = -\frac{1}{\xi}e^{-\frac{x}{\xi}}$) tend to infinity as x and ξ approach zero with fixed values of x/ξ ; similar unbounded behavior arises for other derivatives of this function with respect to x and/or ξ . As in the case of the square-root function considered above, changes of variables can be utilized to resolve the x near-singularity of the complete family. As a simple preliminary illustration we note that, under the change of variables

$$x = x(v) = \frac{e^v}{e^v + 1}, \quad (16)$$

the family $w_\xi(x(v)) = 1 - e^{-\frac{x(v)}{\xi}}$ has uniformly bounded derivatives with respect to v . Indeed, for the first derivative, for example, we obtain

$$\frac{d}{dv} w_\xi(x(v)) = -(1 - x(v)) \frac{x(v)}{\xi} e^{-\frac{x(v)}{\xi}},$$

which is uniformly bounded, for all v and ξ , on account of the boundedness of the functions $(1 - x(v))$ and Xe^{-X} with $X = \frac{x(v)}{\xi}$. A similar calculation shows that all of the v derivatives of $w_\xi(x(v))$ are uniformly bounded. Use of an additional order- n algebraic change of variables $\xi = \Psi(r)$, finally, ensures that the derivatives with respect to v of all orders, and the derivatives with respect to r up to order $(n - 1)$ are uniformly bounded—for all v and r .

As mentioned above, the change of variables we use to treat the Fresnel boundary-layer singularity expressed in Eq. (14) is related to but different from the simple algebraic transformation $\xi = r^n$ discussed previously. Like the simple transformation, the alternative algebraic transformation we use induces a mesh grading via a power- n expression which maintains an adequate number of discretization points away from the finely graded region next to the singular point (which corresponds to $\xi = r = 0$ in the simple $\sqrt{\xi}$ example considered above). In detail, instead of $\xi = r^n$, in this paper we use rescaled versions [via linear functions $s = s(r)$] of the algebraic Martensen-Kussmaul (MK) change of variables [39] given by

$$h_N(s) = 2\pi \frac{[v(s)]^N}{[v(s)]^N + [v(2\pi - s)]^N}, \quad 0 \leq s \leq 2\pi,$$

$$v(s) = \left(\frac{1}{N} - \frac{1}{2}\right) \left(\frac{\pi - s}{\pi}\right)^3 + \frac{1}{N} \frac{s - \pi}{\pi} + \frac{1}{2}.$$

Roughly speaking, this transformation accumulates one half of the grid points toward the endpoints 0 and 2π , while the other half is distributed fairly uniformly within the interior of the interval $[0, 2\pi]$. In the context of angular boundary-layer resolution we utilize this transformation with two different values of N , in conjunction with the linear rescaling

$$s = s(r) = \begin{cases} \pi \frac{r}{\xi_c^0} & \text{for } 0 < r \leq \xi_c^0, \\ \pi \frac{r - \xi_c^0}{1 - \xi_c^0} & \text{for } \xi_c^0 < r \leq 1. \end{cases} \quad (17)$$

In detail, in view of the relation (7), we introduce the angular change of variables

$$\xi = \Psi(r) = \begin{cases} \psi(r) & \text{for } 0 \leq r \leq 1, \\ -\psi(-r) & \text{for } -1 \leq r < 0, \end{cases} \quad (18)$$

where, for a given value n (taken to equal $n = 3.2$ throughout this paper),

$$\psi(r) = \begin{cases} \frac{h_n(s(r))}{\pi} \xi_c^0, & 0 < r \leq \xi_c^0, \\ \xi_c^0 + \frac{1 - \xi_c^0}{\pi} h_2(s(r)), & \xi_c^0 < r \leq 1. \end{cases} \quad (19)$$

Note that this change of variables results in a numerical grid in the ξ variable that is refined near $\xi = 0$ and $\xi = \pm \xi_c^0$; as shown in the following section, such graded refinements provide the necessary resolution of boundary layers. As discussed in the following section, the function h_2 , that is to say, h_N with $N = 2$, which is used in the case $\xi_c^0 < r \leq 1$ of definition (19), exactly cancels the square-root singularity (15) in the Fresnel coefficient. The function h_N with $N = n$ used for the case $0 < r \leq \xi_c^0$, in turn, is utilized to smoothen the singularity of the solution u near $\xi = 0$. A different use of the MK function $h_N(s)$ is made in Sec. V A, with a different linear rescaling, to adequately discretize a collimated boundary source.

The formal analyses presented in the following section for both the angular and spatial regularization processes is based on use of the convergent Neumann series representation [1,40]

$$u(x, \xi) = \sum_{m=0}^{\infty} u^m(x, \xi), \quad (20)$$

of the solution u , where $u^m(x, \xi) = K^m[g + L[q]](x, \xi)$ is defined in Appendix A as the result of the action of the m th power K^m of a certain operator K on a “boundary-condition” function g as well as the result $L[q]$ of the action of an operator L on the source function q in Eq. (1). Physically, $u^m(x, \xi)$ represents the density of photons at point x traveling with direction given by ξ that have undergone a number m of collision and scattering events.

As is often the case in practice [and as established in Appendix B for the 1D Henyey-Greenstein phase function given in Eqs. (44) and (45)], the phase function $p = p(\xi, \xi')$ and its derivatives are assumed to be bounded: for each integer $j \geq 0$ there exists a constant $C_j > 0$ such that

$$\left| \frac{\partial^j}{\partial \xi^j} p(\xi, \xi') \right| < C_j \quad \text{for } -1 \leq \xi, \xi' \leq 1. \quad (21)$$

It follows that provided $u = u(x, \xi)$ is a bounded function of x and ξ (as it generally may be expected on physical grounds), for each integer $j \geq 0$ there exists a constant $D_j > 0$ such

that for $-1 \leq \xi \leq 1$ and $0 \leq x \leq 1$ we have for the collision integral (2)

$$\left| \frac{\partial^j}{\partial \xi^j} \Phi(x, \xi) \right| < D_j, \quad (22)$$

a fact that will be exploited in the theoretical study of angular boundary layers presented in Sec. III C. Similarly, defining

$$\Phi^m(x, \xi) = \int_{-1}^1 p(\xi, \xi') u^m(x, \xi') d\xi', \quad (23)$$

we may generally assume

$$\left| \frac{\partial^j}{\partial \xi^j} \Phi^m(x, \xi) \right| < E_j^m, \quad (24)$$

for certain constants E_j^m . Naturally, our formal study of solution smoothness under the changes of variables introduced above assumes that the boundary sources $\ell_0(\xi)$ and $\ell_1(\xi)$ and the interior source $q(x, \xi)$ are smooth functions, with bounded derivatives of all orders, with respect to x and ξ . For notational simplicity we present proofs for the case of spatially constant absorption and scattering coefficients, $\mu_a(x) = \mu_a$, $\mu_s(x) = \mu_s$, and $\mu_t(x) = \mu_t = \mu_a + \mu_s$.

C. Boundary-layer regularization I: Angular regularization

This section shows that the change of variables (19) regularizes the exponential and algebraic boundary layers [namely, the quantities (A2) and (A3) that, in view of Eqs. (A7) through (A11), are a part of the terms (A11) of the Neumann expansion (A9) of the solution, see also Fig. 7] that occur in the integrand $p(\xi, \xi') u(x, \xi')$ of the collision integral (2), with respect to the integration variable ξ' for ξ' around $\xi' = 0$. (Without loss of generality we restrict our proof to the case $\xi > 0$; the case $\xi < 0$ follows analogously.) More precisely, the results in this section show that the collision integrand that results upon the change of integration variables $\xi' = \psi(r)$, namely, $[p(\xi, \psi(r)) u(x, \psi(r)) \frac{d\psi}{dr}(r)]$, has bounded derivatives ∂_r^j with respect to r , of orders $j \leq (n-1)$ for $0 \leq r \leq 1$ and for all $x, 0 \leq x \leq 1$ —and, thus, integration of this integrand on the basis of, e.g., the Gauss-Legendre rule gives rise to high-order convergence, of orders consistent with classical error estimates [41] for the Gauss-Legendre quadrature rule: the ℓ -point Gauss-Legendre quadrature error decreases like $32V/[15\pi(n-1)(2\ell-n+2)^{n-1}]$ for $\ell \geq \frac{n-1}{2}$, provided the derivatives of the integrated function up to order $(n-1)$ are bounded by the constant $V > 0$. Since, in the present case $\xi \geq 0$ the function $u(x, \xi)$ has bounded derivatives outside a half-neighborhood of $\xi = 0$ to the right of $\xi = 0$ and a half neighborhood of $\xi = \xi_c^0$ to the right of $\xi = \xi_c^0$ (see Fig. 7), we show that under the composition $u(x, \psi(r))$ the resulting integrand has bounded derivatives of order $0 \leq j \leq (n-1)$, for $0 \leq r \leq 1$, in both, half-neighborhoods of $r = 0$ and $r = \xi_c^0$ to the right of $r = 0$ and $r = \xi_c^0$, respectively.

We establish first the derivative boundedness near $r = 0$ and to the right of this point. To do this, noting that the change of variables (19) behaves asymptotically like the n th power function, $\psi(r) \sim r^n$, as $r \rightarrow 0^+$, it suffices to show that the change of variables $\xi' = \zeta_1(r) = r^n$ results in the desired bounded integrand derivatives for the region $0 \leq r < \xi_c^0$ and

up to and including $r = \xi_c^0$ from the left. Under the present hypothesis Eq. (21) that the phase function $p(\xi, \xi')$ has bounded derivatives, and since $\zeta_1'(r) = nr^{n-1}$, it suffices to show that $\frac{\partial^j}{\partial r^j}(u(x, r^n)r^{n-1})$ is bounded for $0 \leq r < \xi_c^0$ and up to and including $r = \xi_c^0$ from the left, and for $0 \leq j \leq (n-1)$. We do this by showing, by induction in m , that the same is true for each term u^m in the Neumann series (20) of u . That is to say that for some positive constant A_j , we show inductively that

$$\frac{\partial^j}{\partial r^j}(u^m(x, r^n)r^{n-1}) < A_j, \quad 0 \leq j \leq n-1, \quad (25)$$

and thus, the j th derivative of the integrand in the scattering integral is bounded for such values of r and j .

Proof of Eq. (25). We first consider the case $m = 0$ for which, in view of Eqs. (A1), (A2), and (A11) in Appendix A, $\partial^j/\partial r^j(u^0(x, r^n)r^{n-1})$ equals

$$\frac{\partial^j}{\partial r^j}(\ell_0(r^n)e^{-\mu_t x/r^n} r^{n-1} + L[q](x, r^n)r^{n-1}), \quad (26)$$

and we consider, in turn, each one of the two terms on the right-hand side of Eq. (26). In regard to the first right-hand term, given that, by assumption, the boundary source term $\ell_0(\xi)$ has bounded derivatives of all orders, it suffices to show that $e^{-\mu_t x/r^n} r^{n-1}$ has bounded derivatives for the relevant orders of differentiation. Using Eqs. (A12) and (A13), and calling $X = \mu_t x/r^n$ we obtain the expression

$$\frac{\partial^j}{\partial r^j}(e^{-\mu_t x/r^n} r^{n-1}) = r^{n-j-1} \sum_{\ell=0}^j \sum_{s=0}^{j-\ell-1} a_{\ell,s} X^{j-\ell-s} e^{-X}, \quad (27)$$

with real coefficients $a_{\ell,s}$. Since, for any real constant $M \geq 0$,

$$X^M e^{-X} \text{ is bounded for all } X \geq 0, \quad (28)$$

and since all of the exponents $(n-j-1)$ on the right-hand side of the equation are nonnegative for $0 \leq j \leq (n-1)$, it follows that the left-hand quantity in Eq. (27) is bounded for this range of values of j , as desired. For the second term in Eq. (26), in turn, using Eq. (A2) in the case $\xi > 0$ considered presently, together with Eq. (A16), we obtain

$$\begin{aligned} & \frac{\partial^j}{\partial r^j}(L[q](x, r^n)r^{n-1}) \\ &= r^{n-j-1} \sum_{k=0}^j \sum_{\ell=1}^j \sum_{s=1}^{j-k} \alpha_{j,k,\ell,s} r^{sn} \\ & \quad \times \int_0^x \frac{\partial^s q}{\partial \xi^s}(y, r^n) \left[\frac{\mu_t(y-x)}{r^n} \right]^\ell e^{-\mu_t(y-x)/r^n} dy, \end{aligned} \quad (29)$$

for certain coefficients $\alpha_{j,k,\ell,s}$. Then, using Eq. (28) with $X = \mu_t(y-x)/r^n$, and since, by hypothesis, the source term $q(y, \xi)$ has bounded derivatives, it follows that the integrand on the right-hand side of Eq. (29), and, thus, the complete right-hand side, is also bounded for all $0 \leq j \leq n-1$ and for $0 \leq r \leq \xi_c^0$. The $m = 0$ case of the inductive proof has thus been concluded.

To complete the inductive proof in the present case (in the r region to the left of $r = \xi_c^0$), we assume that for a given m the derivatives $\partial_r^j(r^{n-1}u^m)$ are bounded for $0 \leq j \leq (n-1)$, and we show that the same is true for the derivatives $\partial_r^j(r^{n-1}u^{m+1})$,

or, equivalently, in view of Eq. (A7) through (A11), that the terms

$$\frac{\partial^j}{\partial r^j} (\mathcal{R}^0(r^n)u^m(0, -r^n)e^{-\mu_t x/r^n} r^{n-1})$$

and

$$\frac{\partial^j}{\partial r^j} (\mu_s L[S[u^m]](x, r^n) r^{n-1}) \quad (30)$$

are bounded for $0 \leq j \leq (n-1)$. By the induction hypothesis and in view of Eqs. (27) and (28) we see that the first term derivatives are bounded for $0 \leq j \leq (n-1)$. For the second term, in turn, using once again Eq. (A2), in conjunction with Eqs. (A4), (A16), and (23), we obtain

$$\begin{aligned} & \frac{\partial^j}{\partial r^j} (L[S[u^m]](x, r^n) r^{n-1}) \\ &= r^{n-j-1} \sum_{k=0}^j \sum_{\ell=1}^j \sum_{s=0}^{j-k} \alpha_{j,k,\ell,s} r^{sn} \\ & \quad \times \int_0^x \frac{\partial^s \Phi^m}{\partial \xi^s}(y, r^n) \left[\frac{\mu_t(y-x)}{r^n} \right]^\ell e^{-\mu_t(y-x)/r^n} dy. \end{aligned}$$

In view of Eq. (24) together with the bound (28) with $X = \mu_t(y-x)/r^n$ we see that the integrand on the right-hand side is bounded, and, thus that, for $0 \leq j \leq (n-1)$, so is the complete second term in Eq. (30).

Having established the integrand derivative boundedness under the change of variables (19) in the region $0 \leq r < \xi_c^0$ and up to and including $r = \xi_c^0$ from the left, we now proceed to establish the corresponding boundedness in the remaining region $\xi_c^0 < r \leq 1$ up to and including $r = \xi_c^0$ from the right—in which the change of variables (19) behaves asymptotically like $\psi(r) \sim \xi_c^0 + b(r - \xi_c^0)^2$ as $r \rightarrow \xi_c^0$ from the right for a certain real constant b . In view of this asymptotic character, it suffices to show that under the change of variables $\xi' = \zeta_2(r) = \xi_c^0 + b(r - \xi_c^0)^2$, the j th derivative $\frac{\partial^j}{\partial r^j} (u(x, \zeta_2(r)) \frac{d\zeta_2(r)}{dr})$ is bounded for $\xi_c^0 \leq r \leq 1$, which we establish, as in the previous case $0 \leq r < \xi_c^0$, by showing, inductively, that the same is true for each Neumann-series term u^m . In other words, we show that

$$\frac{\partial^j}{\partial r^j} \left(u^m(x, \zeta_2(r)) \frac{d\zeta_2(r)}{dr} \right) \quad (31)$$

is bounded for all nonnegative integers m and for $\xi_c^0 < r \leq 1$ up to and including $r = \xi_c^0$ from the right.

Once again, we begin with the case $m = 0$, for which Eq. (31) equals

$$\begin{aligned} & \frac{\partial^j}{\partial r^j} \left(\ell_0(\zeta_2(r)) e^{-\mu_t x/\zeta_2(r)} \frac{d\zeta_2(r)}{dr} \right) \\ & + \frac{\partial^j}{\partial r^j} \left(L[q](x, \zeta_2(r)) \frac{d\zeta_2(r)}{dr} \right), \end{aligned}$$

both of whose terms are clearly bounded since $\xi > \xi_c^0 > 0$. To complete the inductive proof we assume the derivatives (31) are bounded for a certain integer m , and we show that the same is true for $m+1$. To do this we note that, under the ζ_2 change of variables, the j th derivatives of the $(m+1)$ th term of the Neumann expansion equal the sum of the following two

terms:

$$\begin{aligned} & \frac{\partial^j}{\partial r^j} \left(\mathcal{R}^0(\zeta_2(r)) u^m(0, -\zeta_2(r)) e^{-\mu_t x/\zeta_2(r)} \frac{d\zeta_2(r)}{dr} \right) \\ & \text{and} \quad \frac{\partial^j}{\partial r^j} \left(\mu_s L[S[u^m]](x, \zeta_2(r)) \frac{d\zeta_2(r)}{dr} \right). \end{aligned}$$

But, by the induction hypothesis $u^m(x, \zeta_2(r))$ has bounded derivatives with respect to r for $\xi_c < r \leq 1$ up to and including $r = \xi_c^0$ from the right, and, thus, to show that the same is true for $u^{m+1}(x, \zeta_2(r))$ it suffices to show that $\frac{\partial^j}{\partial r^j} \mathcal{R}^0(\zeta_2(r))$ is itself bounded. But, from Eq. (15), for a certain smooth function S we have that

$$\mathcal{R}^0(\zeta_2(r)) = S(\sqrt{b}(r - \xi_c^0))$$

for $\xi_c^0 \leq r \leq 1$. It follows that $\mathcal{R}^0(\zeta_2(r))$ is smooth for $\xi_c^0 < r \leq 1$ and up to and including $r = \xi_c^0$ from the right and, thus the j th derivatives of u^{m+1} are bounded in that region, as desired. The inductive proof is now complete, establishing that

$$\frac{\partial^j}{\partial r^j} \left(p(\xi, \psi(r)) u(x, \psi(r)) \frac{d\psi}{dr}(r) \right)$$

is bounded for all $0 \leq r \leq 1$, $0 \leq x \leq 1$ and $0 \leq j \leq (n-1)$.

D. Boundary-layer regularization II: Spatial regularization

The discussion in this section shows that the change of variables (16) regularizes the solution $u(x, \xi)$ in the both the left and right boundary-layer regions, namely $\frac{\mu_t x}{\xi} < \varepsilon$ ($0 < \xi \leq 1$) and $\frac{\mu_t(x-1)}{\xi} < \varepsilon$ ($-1 \leq \xi < 0$), respectively—which, e.g., for small values of $|\xi|$, are small regions near $x = 0$ and $x = 1$ within the physical domain $0 \leq x \leq 1$. (Here $0 < \varepsilon \lesssim 1$ is an arbitrary number.) In the present context the solution $u(x, \xi)$ is said to be regularized in the sense that the v -derivatives of the composition $u(x(v), \xi)$ of arbitrary order are bounded for all values of v for which $x(v)$ is contained within the left and right boundary-layer regions. This fact is established in this section (using $\varepsilon = 1$ for definiteness) by showing that each term u^m in the Neumann series (A9) has this property, that is to say, for each nonnegative integer j there exists a positive constant B_j such that

$$\left| \frac{\partial^j}{\partial v^j} u^m(x(v), \xi) \right| < B_j \quad (32)$$

for all v and ξ , with $-\infty < v < \infty$ and $|\xi| \leq 1$, such that $(x(v), \xi)$ lies in either of the two boundary-layer regions. As in Sec. III C, without loss of generality we restrict our proof to the case $\xi > 0$; the case $\xi < 0$ follows similarly.

Remark 2. Our spatial regularization proof relies on the fact that all spatial derivatives of the solution u with respect to x are bounded *outside* the boundary-layer regions—i.e., for $\frac{\mu_t x}{\xi} > 1$, $0 < \xi \leq 1$, and for $\frac{\mu_t(x-1)}{\xi} > 1$, $-1 \leq \xi < 0$ —as might be expected from standard asymptotic boundary-layer theory with asymptotic matching [38]. Existing theoretical results in suitable functional spaces [42] only provide limited insights in this regard. But, certainly, computational investigations available in the literature [30,43], as well as our own

high-resolution simulations such as those presented in Fig. 6, computationally demonstrate the needed derivative boundedness outside the boundary-layer regions. A theoretical proof of the away-from-boundary derivative boundedness, which would certainly be valuable, and which could be based on consideration of asymptotics of integrals, is beyond the scope of this paper and is left for future work.

Proof of Eq. (32). The proof is presented in what follows for all nonnegative integers m and j and for spatial and angular points $x(v)$ and ξ in the left boundary-layer region $|X| = |\mu_t x(v)/\xi| < 1$, $\xi > 0$ (the proof in the right boundary layer $|\mu_t(x(v) - 1)/\xi| < 1$, $\xi < 0$ is analogous). Proceeding by induction in m we thus first consider the j th derivative in the case $m = 0$ which, in view of Eq. (A10), is

given by

$$\ell_0(\xi) \frac{\partial^j}{\partial v^j} e^{-\mu_t x(v)/\xi} + \frac{\partial^j}{\partial v^j} L[q](x(v), \xi). \quad (33)$$

Using $X = \frac{\mu_t x(v)}{\xi}$ and Eq. (A18), the first term in Eq. (33) is seen to equal

$$\ell_0(\xi) e^{-X} \sum_{k=1}^j \sum_{\ell=0}^j b_{k,\ell} X^k x(v)^\ell \quad (34)$$

for some real coefficients $b_{k,\ell}$; clearly, in view of Eq. (28) this term is bounded for all relevant values of (v, ξ) . Integrating by parts $j + 1$ times and utilizing Eq. (A20), for the second term we obtain

$$\begin{aligned} \frac{\partial^j}{\partial v^j} L[q](x(v), \xi) &= \sum_{\ell=1}^{j+1} (-1)^{\ell-1} \frac{\xi^{\ell-1}}{\mu_t^\ell} \frac{\partial^j}{\partial v^j} \left(\frac{\partial^{\ell-1}}{\partial x^{\ell-1}} q(x(v), \xi) - e^{-\mu_t x(v)/\xi} \frac{\partial^{\ell-1}}{\partial x^{\ell-1}} q(0, \xi) \right) + (-1)^{j+1} \frac{\xi^j}{\mu_t^{j+1}} \left[e^{-\mu_t x(v)/\xi} \right. \\ &\times \sum_{m=1}^j \left(\frac{\mu_t x(v)}{\xi} \right)^m \sum_{\ell=0}^j b_{m,\ell} x(v)^\ell \int_0^{x(v)} e^{\mu_t y/\xi} \frac{\partial^{j+1}}{\partial y^{j+1}} q(y, \xi) dy + \sum_{m=1}^j \sum_{\alpha=1}^{j-m} \sum_{\beta=0}^{j-m-\alpha} \sum_{s=0}^{j-m-\alpha-\beta} \sum_{\gamma=1}^{j-m-\alpha-\beta-s} \sum_{\delta=0}^{j-m-\alpha-\beta-s-\gamma} a_{j,m,\alpha,\beta,\gamma,\delta} \\ &\left. \times \left(\frac{\mu_t x(v)}{\xi} \right)^{\alpha+\gamma} x(v)^{\beta+\delta} \frac{\partial^s}{\partial v^s} \left(\frac{\partial^{j+1}}{\partial x^{j+1}} q(x(v), \xi) \frac{dx(v)}{dv} \right) \right]. \end{aligned}$$

Since, by assumption, the function q is smooth, with, say, $|\frac{\partial^\ell}{\partial x^\ell} q(x, \xi)| < C_\ell$ for each integer ℓ and all relevant values of x and ξ , we have

$$\left| \int_0^x e^{\mu_t y/\xi} \frac{\partial^\ell}{\partial y^\ell} q(y, \xi) dy \right| \leq C_\ell \frac{\xi}{\mu_t} (e^{\mu_t x/\xi} - 1),$$

which, upon substitution in the previous expression with $\ell = j + 1$, presents $\frac{\partial^j}{\partial v^j} L[q](x(v), \xi)$ as a sum of terms containing nonnegative powers of the bounded quantities ξ , $x(v)$, as well as derivatives of $x(v)$ and derivatives of q , all of which are also uniformly bounded.

To complete the inductive proof we assume that, for all integers j , the j derivative $\partial_v^j u^m$ of the m th Neumann series term u^m is bounded in the boundary-layer regions, and we show that the same is true for the $(m + 1)$ th term u^{m+1} . To do this, we first differentiate Eq. (A11) to obtain

$$\frac{\partial^j}{\partial v^j} u^{m+1}(x(v), \xi) = \frac{\partial^j}{\partial v^j} (\mathcal{R}^0(\xi) u^m(0, -\xi) e^{-\mu_t x(v)/\xi}) + \frac{\partial^j}{\partial v^j} (\mu_s L[S[u^m]](x(v), \xi)). \quad (35)$$

The derivatives in the first term on the right-hand side were already shown to be bounded as part of the $m = 0$ proof [cf. Eq. (34) and associated text]. For the second right-hand term, in turn, using Eqs. (23) and (A21) with $f = \Phi^m$ we obtain

$$\begin{aligned} \frac{\partial^j}{\partial v^j} L[S[u^m]](x(v), \xi) &= \sum_{k=1}^j \sum_{w,\alpha=1}^{j-k} \sum_{s=0}^{k-1} \sum_{\beta=0}^{k-s-1} \sum_{\ell=0}^s \sum_{\delta,\gamma=1}^{s-\ell} d_{j,k,w,\alpha,\beta,\delta,\gamma,s,\ell} \frac{X^{\delta+w+1}}{\mu_t} (x(v) - 1)^{k-s-\beta} x(v)^{\alpha+\beta+\gamma} \frac{\partial^\ell}{\partial v^\ell} \Phi^m(x(v), \xi) \\ &+ \frac{e^{-\mu_t x/\xi}}{\xi} \int_0^{x(v)} e^{\mu_t y/\xi} \Phi^m(y, \xi) dy \sum_{k=1}^j X^k \sum_{\ell=0}^j b_{k,\ell}. \end{aligned}$$

In view of the induction hypothesis, Eq. (23) and Remark 2 we see that the ℓ th derivative term on the right-hand side of this equation is bounded. Since $\Phi^m(y, \xi)$ is also bounded [$j = 0$ in Eq. (24)], however, we see that

$$\int_0^{x(v)} e^{\mu_t y/\xi} \Phi^m(y, \xi) dy \leq E_0^m x(v) e^{\mu_t x(v)/\xi},$$

for some constant E_0^m which, upon substitution on the right-hand produces a term bounded by a constant time $|X|$. Since

$|x(v)| \leq 1$, it follows that the right-hand side in this equation is bounded by a linear combination of powers of $|X|$. Since additionally $|X| < 1$ in the boundary-layer region, it follows that the left-hand side in Eq. (35) is bounded in the boundary-layer region as well, and the proof is complete.

Figure 6 illustrates this result by displaying the (clearly bounded) v derivatives for a numerical solution of the full transport problem in the complete spatioangular domain. A generalization of this result to the case of spatially varying

parameters $\mu_s(x)$, $\mu_a(x)$, and $\mu_t(x)$ proceeds similarly, provided the derivatives of these functions are adequately bounded.

IV. NUMERICAL METHODS

This section introduces numerical methods, based on the theoretical results presented in Secs. III C and III D, for the numerical solution of the time-independent and time-dependent transport problems (1) and (3). Throughout this section, the solution of the transport equation under the changes of vari-

ables (16) and (18) will be denoted either by

$$U(v, r) = u(x(v), \Psi(r)) \quad (36)$$

or by

$$U(v, r, t) = u(x(v), \Psi(r), t), \quad (37)$$

depending on whether the time-independent or time-dependent problem is considered.

A. Transport problem in the (v, r) and (v, r, t) variables

Using Eq. (36), upon application of the changes of variables (16) and (18), the time independent transport problem (1) becomes

$$\begin{aligned} (2 + 2 \cosh(v)) \Psi(r) \frac{\partial}{\partial v} U(v, r) + \mu_t(x(v)) U(v, r) &= \mu_s(x(v)) \int_{-1}^1 p(\Psi(r), \Psi(r')) U(v, r') \frac{d\Psi}{dr}(r') dr' + q(x(v), \Psi(r)), \\ U(-\infty, r) &= \mathcal{R}^0(\Psi(r)) U(-\infty, \Psi^{-1}(\Psi_R(r))) + \ell_0(\Psi(r)), \quad 0 \leq r \leq 1, \\ U(\infty, r) &= \mathcal{R}^1(\Psi(r)) U(\infty, \Psi^{-1}(\Psi_R(r))) + \ell_1(\Psi(r)), \quad -1 \leq r < 0. \end{aligned} \quad (38)$$

A similar expression results under such changes of variables for the time dependent transport problem (3):

$$\begin{aligned} \left[\frac{1}{c} \frac{\partial}{\partial t} + \Psi(r) (2 + 2 \cosh(v)) \frac{\partial}{\partial v} + \mu_t(x(v)) \right] U(v, r, t) &= \mu_s(x(v)) \int_{-1}^1 p(\Psi(r), \Psi(r')) U(v, r', t) \frac{d\Psi}{dr}(r') dr' + q(x(v), \Psi(r), t), \\ U(v, r, t = 0) &= 0, \quad U(-\infty, r, t) = \mathcal{R}^0(\xi) U(-\infty, \Psi^{-1}(\Psi_R(r)), t) + \ell_0(\Psi(r), t), \quad 0 \leq r \leq 1, \\ U(\infty, r, t) &= \mathcal{R}^1(\xi) U(\infty, \Psi^{-1}(\Psi_R(r)), t) + \ell_1(\Psi(r), t), \quad -1 \leq r < 0. \end{aligned} \quad (39)$$

Naturally, Eq. (39) is the relevant equation for time-dependent problems, which, containing transient data information, provides in many cases the most useful model for the solution of the inverse transport problem. Additionally, this equation may be useful even for solution of the time-independent problem—via time relaxation. In detail, considering, e.g., boundary condition functions of the form $\ell_0(\Psi(r), t) = T(t) \ell_0(\Psi(r))$ and $\ell_1(\Psi(r), t) = T(t) \ell_1(\Psi(r))$ [where $T(t)$ denotes a suitable time profile that smoothly transitions from $T(0) = 0$ to $T(t_1) = 1$ for some $t_1 > 0$] and evolving the system up to sufficiently large times $t > t_1$ over several hundred (respectively, several thousand) time steps for low (respectively, large) values of the scattering coefficient μ_s , results in convergence to the desired stationary solution. Alternatively, the time-independent problem can be solved directly on the basis of direct discretization of the time-independent equation (38). The time-relaxation approach, which does not require inversion of the full spatioangular matrix system, does depend on implicit solution of the time-dependent problem for a sufficiently long time period, as described above. While the time-independent-equation approach does not require time evolution, in turn, the computational cost for the inversion of the system matrix grows quickly as the discretization is refined. In practice we have found excellent agreement between the results provided by these approaches for the solution of time-independent problems. Roughly speaking, further, we have found that for high-accuracy and/or low-to-moderate values of μ_s the approach based on the time-dependent equation is preferable, while use of the time-independent

equation is advantageous for large values of the scattering coefficient—which, in the time dependent-equation approach demands long relaxation times.

The proposed discretized version of the time-independent problem (38) can be expressed in the form

$$[\Xi \mathbb{D} + \mu_t \mathbb{I} - \mu_s \mathbb{S}] \tilde{\mathbf{u}} = \tilde{\mathbf{q}}, \quad (40)$$

where \mathbb{D} , Ξ , and \mathbb{S} denote a discrete differential operator in the variable v ; a matrix corresponding to the coefficient $(2 + 2 \cosh(v)) \Psi(r)$ multiplying the v derivative in the equation; and the discretized scattering operator introduced in Eq. (42) below, respectively. The discrete version \mathbb{D} of $\frac{\partial}{\partial v}$ operator is obtained by direct differentiation of Fourier series obtained by means of the Fourier-continuation method (FC) [44–47], which enables representation of general smooth nonperiodic functions by Fourier-series with high accuracy and negligible numerical dispersion. The quantities $\tilde{\mathbf{u}} = (u_{i,m}) \approx (u(x(v_i), \Psi(r_m)))$ and $\tilde{\mathbf{q}} = (q_{i,m}) = (q(x(v_i), \Psi(r_m)))$, in turn, denote the numerical approximation of the solution and the source function at the points $(x(v_i), \Psi(r_m))$, where v_i and r_m denote the discretization points in the v and r variables, respectively: v_i (respectively, r_m) provides a uniform discretization of the domain $-v_{\min} \leq v_i \leq v_{\max}$ (respectively, multi-interval Gauss-Legendre discretizations, as detailed in Sec. IV B).

The discrete scattering operator \mathbb{S} is used to incorporate in the discrete setting the scattering integral Φ displayed in Eq. (2), which occurs on the right-hand side of Eq. (1). In detail, upon application of the change of variables (18)

and (19) and subsequent discretization of the resulting integral using Gauss-Legendre quadrature in the variable r in each of the four intervals implicit in that change of variables, we obtain a discretized version of the collision term which, for a given function $u = u(x, \xi')$, or, more generally, for a possibly time-dependent function $u = u(x, \xi', t)$ as considered below in this section, may be expressed in the form

$$\Phi(x_i, \xi_j, t) \sim \sum_{m=1}^M w_m p(\xi_j, \xi_m) u(x_i, \xi_m, t). \quad (41)$$

Here the weights w_m equal the product of the Gauss-Legendre integration weights and the Jacobian of the change of variables used, and, as indicated above, $x_i = x(v_i)$ and $\xi_k = \Psi(r_k)$. Utilizing the ordering

$$\bar{\mathbf{u}} = [u_{1,1}, \dots, u_{N,1}, \dots, u_{1,M}, \dots, u_{N,M}]^T$$

of the unknowns $\bar{\mathbf{u}} = (u_{i,m})$ for N spatial points and M discrete directions, the scattering integral $\Phi(x_i, \xi_j)$ associated with the approximation $u(x_i, \xi_m) \approx u_{i,m}$ may be expressed in the form $\Phi(x_i, \xi_j) \approx \mathbb{S} \bar{\mathbf{u}}$, where, letting $\mathbb{P}_{m,j} = \text{diag}(w_m p(\xi_j, \xi_m)) \in \mathbb{R}^{N \times N}$, $\mathbb{S} \in \mathbb{R}^{(N \times M)^2}$ denotes the matrix

$$\mathbb{S} = \begin{bmatrix} \mathbb{P}_{1,1} & \dots & \mathbb{P}_{M,1} \\ \vdots & \ddots & \vdots \\ \mathbb{P}_{1,M} & \dots & \mathbb{P}_{M,M} \end{bmatrix}. \quad (42)$$

The proposed numerical solver for the time-dependent problem (39), which discretizes time on the basis of the (implicit) third-order backward differentiation formula (BDF3) [48, Ch. 3.12], amounts to an implicit version of the FC-DOM method [28,49] that additionally incorporates the changes of variables inherent in Eq. (39) as well as the phase-function treatment described in Sec. IV B. As described in what follows, further, to avoid the joint-inversion of a spatioangular discretization matrix as well as the application of the inverse matrix at each time step, the proposed algorithm evaluates the collisional term and Fresnel boundary conditions by utilizing third-order polynomial extrapolation. In detail, let $t^n = n\Delta t$, $u_{i,j}^n \sim u(x(v_i), \xi_j, t^n)$, and for $j = 1, \dots, M$, $u_j^n = (u_{i,j}^n)_{i=1}^N$. Then, using the $\mathbb{R}^{N \times N}$ versions (one ξ_j at a time) $\hat{\mathbb{I}}$ and $\hat{\mathbb{D}}$ of the identity operator \mathbb{I} and the FC-based spatial differential operator \mathbb{D} used in the time independent case, the resulting discrete version of Eq. (39) can be expressed in the form

$$\begin{aligned} & [\hat{\mathbb{I}} + \beta \Delta t \xi_j (2 + 2 \cosh(v)) \hat{\mathbb{D}} + \beta \Delta t \mu_t \hat{\mathbb{I}}] u_j^{n+1} \\ &= \sum_{k=0}^2 \alpha_k u_j^{n-k} + \beta \Delta t \mu_s \tilde{\Phi}_j^{n+1} + \beta \Delta t q_j^{n+1}, \end{aligned}$$

where α_k and β are the BDF3 coefficients. Here $\tilde{\Phi}_j^{n+1}$ denotes a numerical value of the scattering integral (2) obtained by the substitution $u = \tilde{u}_{i,j}^{n+1}$, where

$$\tilde{u}_{i,j}^{n+1} = \sum_{k=0}^2 (-1)^k \binom{3}{k+1} u_{i,j}^{n-k}$$

equals the third order-accurate polynomial extrapolation of the solution values $u_{i,j}^{n-k}$ for $0 \leq k \leq 2$. This extrapolated solution value is also used to evaluate the right-hand sides

of the Fresnel boundary condition terms in Eq. (3). As suggested above, the use of these extrapolated quantities leads to significant dimensionality reductions, from dimension NM to dimension N , in the linear operator that needs to be inverted and applied for the time evolution under the implicit BDF3 algorithm—while preserving the accuracy order and time-stability inherent in the BDF3 algorithm—and thus results in very significant efficiency gains without loss of accuracy and without stringent CFL restrictions.

B. Scattering operator and efficient treatment of anisotropic scattering

Viewing the problems (1) and (3) as 3D problems in the infinite slab $0 \leq x \leq 1$, $-\infty < y, z < \infty$ with rotational invariance around the $\hat{x} = (1, 0, 0)$ direction (that is, with invariance in the azimuthal variable φ around the x axis) and with translation invariance along the $\hat{y} = (0, 1, 0)$ and $\hat{z} = (0, 0, 1)$ directions, we denote by

$$\hat{\omega}(\xi, \varphi) = \xi \hat{x} + \cos(\varphi) \sqrt{1 - \xi^2} \hat{y} + \sin(\varphi) \sqrt{1 - \xi^2} \hat{z},$$

the 3D unit vector in the direction determined by the angles φ and θ , where, letting θ denote the polar angle (i.e., the angle between $\hat{\omega}$ and the x axis) adopting the notation used in previous sections, we set $\xi = \cos(\theta)$. To model the anisotropic scattering of photons within the medium we employ the Henyey-Greenstein phase function

$$\eta = \frac{1 - g^2}{4\pi (1 + g^2 - 2g\hat{\omega}(\xi, \varphi) \times \hat{\omega}(\xi', \varphi'))^{3/2}}, \quad (43)$$

where $\hat{\omega}(\xi, \varphi)$ and $\hat{\omega}(\xi', \varphi')$ indicate the incident and outgoing directions of photons undergoing a scattering event, and where g denotes the anisotropy factor. Note that since $\hat{\omega}(\xi, \varphi) \times \hat{\omega}(\xi', \varphi') = \xi \xi' + \sqrt{(1 - \xi^2)(1 - \xi'^2)} \cos(\varphi - \varphi')$ we have $\eta = \eta(\xi, \xi', \varphi - \varphi')$. The phase function (43) has been shown to accurately describe scattering interactions in biological tissue, with a typical anisotropy-factor value around $g = 0.9$ [50–53].

In the 3D slab context introduced above, the scattering integral resulting from use of the Henyey-Greenstein phase function (43) is given by

$$\Phi(x, \xi) = \int_{-1}^1 d\xi' u(x, \xi') \int_0^{2\pi} \eta(\xi, \xi', \varphi - \varphi') d\varphi',$$

where the fact that Φ is independent of φ , as suggested by the notation in this equation, follows from the facts that, under the azimuthal invariance inherent in the slab geometry, the angular flux u does not depend on the azimuthal angle [1, Ch. 2], and that owing to the $\cos(\varphi - \varphi')$ dependence of the phase function η , the integral of η with respect to φ' does not depend on φ either. The 1D phase function can thus be defined by

$$p(\xi, \xi') = \int_0^{2\pi} \eta(\xi, \xi', \varphi - \varphi') d\varphi'. \quad (44)$$

Calling $\alpha(\xi, \xi', g) = 1 + g^2 - 2g\xi\xi'$ and $\beta(\xi, \xi', g) = 2g\sqrt{1 - \xi^2}\sqrt{1 - \xi'^2}$, we obtain [54, p. 182]

$$\begin{aligned} p(\xi, \xi') &= \frac{1 - g^2}{4\pi} \int_0^{2\pi} \frac{d\varphi'}{\sqrt{(\alpha - \beta \cos(\varphi'))^3}} \\ &= \frac{1 - g^2}{\pi(\alpha - \beta)\sqrt{\alpha + \beta}} E\left(\sqrt{\frac{2\beta}{\alpha + \beta}}\right), \end{aligned} \quad (45)$$

where E denotes the complete elliptic integral of the second kind [54, p. 860].

Using the change of variables $\xi' = \Psi(r)$ [cf. Eq. (18)] we obtain

$$\Phi(x, \xi) = \sum_{i=1}^3 \int_{a_i}^{b_i} p(\xi, \Psi(r)) u(x, \Psi(r)) \frac{d\Psi}{dr} dr, \quad (46)$$

where a_i and b_i ($i = 1, \dots, 3$) denote the endpoints of each one of the subintervals in the partition $\Psi \in [-1, -\xi_c^0] \cup [-\xi_c^0, \xi_c^0] \cup [\xi_c^0, 1]$ of the integration interval $[-1, 1]$ —which is used in our algorithm to avoid integration over points of discontinuity of the integrand, which would result in poor convergence of the corresponding discrete quadrature methods.

It is important to note that, for the values of g close to 1 that generally arise in the context of modeling of biological tissue, the 1D phase function (45) is highly peaked for $(\xi - \xi')$ close to zero [since so is Henyey-Greenstein phase function for $(\xi - \xi', \varphi - \varphi')$ is close to $(0, 0)$], and, thus, for such values of g , the direct numerical evaluation of the scattering integral $\Phi(x, \xi)$ with any reasonable accuracy requires use of a large number of discretization points—each one of which gives rise to a new unknown in the resulting discrete system. To avoid such a computational burden, we propose an approach based on use of a Legendre polynomial expansion in conjunction with a certain precomputation strategy. In detail, for an appropriately selected positive integer L , the proposed approach is based on consideration of the L th order Legendre approximation

$$u(x, \Psi(r)) \frac{d\Psi}{dr} \approx \sum_{n=0}^L \sum_{i=1}^3 c_n^i(x) P_n(\zeta^i(r)), \quad (47)$$

of the integrand factor $u(x, \Psi(r)) \frac{d\Psi}{dr}$ in Eq. (46) for each one of the integration intervals used, where P_n denotes the Legendre polynomial of order n , and where $\zeta^i : [a_i, b_i] \rightarrow [-1, 1]$, $\zeta^i(r) = \frac{2r - a_i - b_i}{a_i - b_i}$, is the linear mapping from the integration interval to the domain of definition of the Legendre polynomials, namely, the interval $[-1, 1]$.

In view of the classical expression for the Legendre coefficients [55], it is easy to check that the coefficients in Eq. (47) are given by

$$c_n^i(x) = \left(\frac{2n+1}{b_i - a_i}\right) \int_{a_i}^{b_i} u(x, \Psi(r)) \frac{d\Psi}{dr} P_n(\zeta^i(r)) dr.$$

Then, substituting Eq. (47) into Eq. (46) yields

$$\Phi(x, \xi) \sim \sum_{n=0}^L \sum_{i=1}^3 c_n^i(x) \Omega_n^i(\xi), \quad (48)$$

with coefficients

$$\Omega_n^i(\xi) = \int_{a_i}^{b_i} p(\xi, \Psi(r)) P_n(\zeta^i(r)) dr, \quad (49)$$

which can be precalculated with limited overall computational effort [since $\Omega_n^i(\xi)$ does not depend on either x or t], even for highly peaked phase functions p (i.e., for $|g|$ close to one). Once obtained, the coefficients $\Omega_n^i(\xi)$ can be used multiple times to evaluate Eq. (46) for all x and t in the computational domain, merely on the basis of the Legendre coefficients $c_n^i(x)$ —whose calculation, only requires an integration grid adequate for resolution of the variation of the integrand for given initial conditions, boundary conditions and source function, but independently of the value of the anisotropy coefficient g . In our implementation, the coefficients $\Omega_n^i(\xi)$ are themselves evaluated by means of the Gauss-Legendre quadrature rule, using sufficiently many discretization points to adequately resolve the (potentially highly peaked) phase function. For example, for the anisotropy coefficient $g = 0.95$ and using an angular integration grid (in the ξ variable) containing $M = 40$ points, the coefficients $\Omega_n^i(\xi)$ were obtained with a relative error of 1.7×10^{-9} by means of an 2000-point Legendre rule in the variable r for all polynomials up to order $L = 8$. The proposed strategy provides a rigorous and efficient computational approach for the resolution of numerical issues widely discussed in the literature, and typically referred to as “false scattering” [56–58].

V. NUMERICAL RESULTS

This section illustrates the character of the proposed solvers, showcasing, in particular, their speed and accuracy as well as their ability to effectively resolve the boundary-layer structures identified in Sec. II as well as the highly peaked anisotropic phase functions [Eqs. (43) through (45)] that are found often in practice. In detail, using the 1D problems (1) and (3) as testbeds for the proposed techniques, this section presents results demonstrating, (i) the accuracy and efficiency that results from the proposed changes of spatial and angular variables (Secs. VA and VB); (ii) the geometrical structure of boundary layers under vacuum, incidence and Fresnel boundary conditions, as well as the effects produced by the proposed changes of variables on the boundary-layer geometry (Sec. VC); and (iii) excellent agreement between simulated and experimental data (Sec. VD).

A. Numerical convergence

For accuracy assessments we utilize numerical convergence tests for a generic scattering medium with absorption coefficient $\mu_a = 0.1/\text{cm}$, scattering coefficient $\mu_s = 10/\text{cm}$, anisotropy factor $g = 0.8$ and refractive index $n_\Omega = 1.33$, surrounded by vacuum ($n_s = 1$). We solve the time-dependent transport problem Eq. (3) with $q = 0$ and with $\ell_0 = \ell_1 = T(t)$ [where $T(t)$ denotes a smooth step function that transitions from 0 to 1, over the time interval $0 \leq t \leq t_f$], up to time $t_f/2$ [at which the slope of the step function $T(t)$ is largest] and for various spatial mesh sizes Δv , time step Δt , number M of discrete directions ξ_j and orders L of the Legendre polynomial expansion (47) that underlies the scattering integral

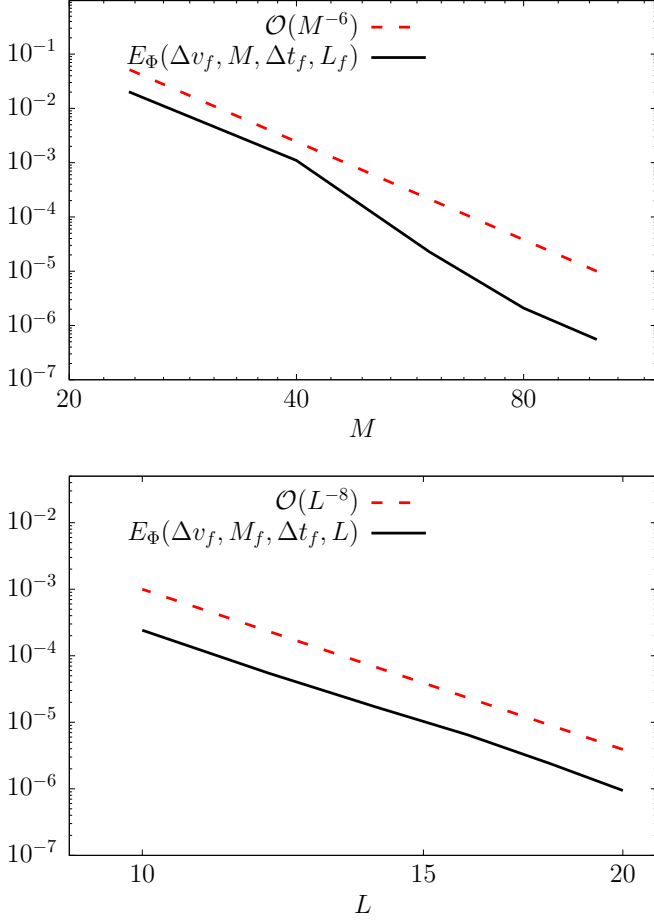


FIG. 2. Convergence of the proposed linear-transport algorithm with boundary-layer resolution. Solid curves: error E_Φ [Eq. (50)]; dashed curves: order of convergence lines. Top panel: $E_\Phi(\Delta v_f, M, \Delta t_f, L_f)$ as a function of the number M of angular discretization points in Eq. (41). Bottom panel: error $E_\Phi(\Delta v_f, M_f, \Delta t_f, L)$ as a function of the order L in the Legendre expansion (47). Here Δv_f , M_f , Δt_f , and L_f denote the fine-grid values listed in the text.

expression (48). To estimate the accuracy of the method we consider the error quantities

$$E_\Phi = E_\Phi(\Delta v, M, \Delta t, L) = \max_{v,r} |\Phi_g(x(v), \Psi(r)) - \Phi_f(x(v), \Psi(r))|, \quad (50)$$

in the grid values Φ_g of the scattering integral (evaluated by comparison with the corresponding fine-grid scattering-integral values Φ_f), as well as the error

$$E_U = E_U(\Delta v, M, \Delta t, L) = \max_{v,r} |U_g(v, r) - U_f(v, r)|, \quad (51)$$

in the grid solution U_g of the angular flux (evaluated by comparison with the corresponding fine-grid angular-flux values U_f). The fine-grid values Φ_f and U_f were obtained using the grid parameters $\Delta v_f = 5 \times 10^{-2}$, $M_f = 200$, $\Delta t_f = 2.5 \times 10^{-3}$, and $L_f = 40$.

The top (respectively, bottom) panel of Fig. 2 displays the error E_Φ as a function of M (respectively, as a function of L),

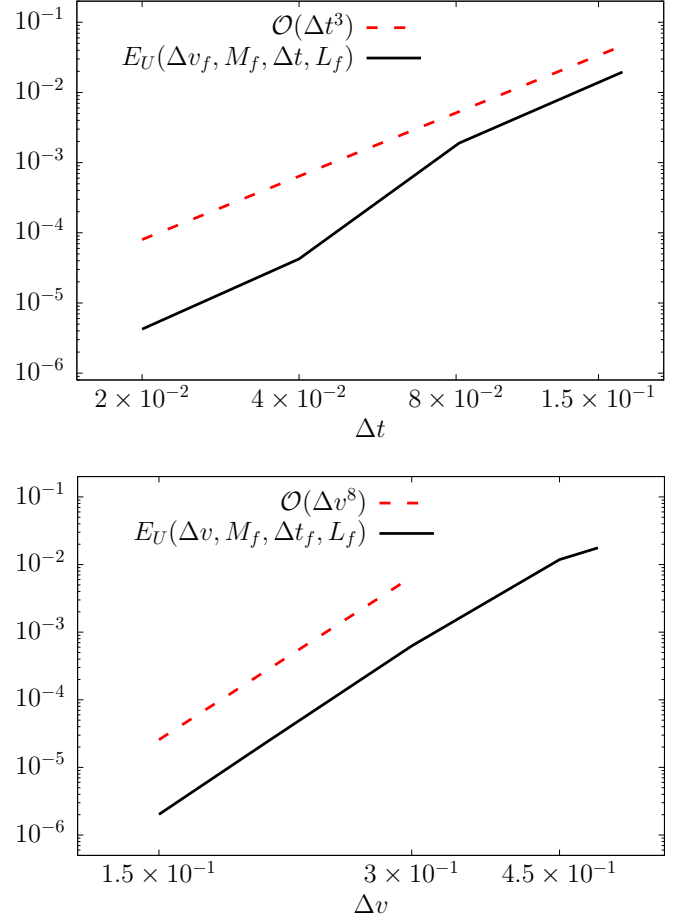


FIG. 3. Same as Fig. 2 but for the error E_U [Eq. (51)] in the angular flux instead of E_Φ . Top panel: error $E_U(\Delta v_f, M_f, \Delta t, L_f)$ as a function of the time step Δt . Bottom panel: Error $E_U(\Delta v, M_f, \Delta t_f, L_f)$ as a function of the spatial mesh size Δv .

with all other mesh sizes set to the fine-grid values. Similarly, the top (respectively, bottom) panel of Fig. 3 presents the error E_U as a function of Δt (respectively, Δv), with all other mesh sizes once again set to the fine-grid values. Taken as a set, the results in Figs. 2 and 3 illustrate that under the boundary-layer resolution achieved via the spatial and angular changes of variables introduced in Sec. III B and illustrated in Fig. 6 (cf. Fig. 5) the proposed algorithms in the (v, ξ, t) variables achieve high orders of convergence. Additionally, the top panel in Fig. 2 shows that use of the expansion (47) together with the precomputations (49) produces the rapidly convergent expression (48) for the scattering integral Φ even in presence of a strongly peaked Henyey-Greenstein phase function p .

B. Time-domain simulation with collimated pulsed beams

This section demonstrates the performance of the proposed linear-transport and radiative-transfer solver in the context of one of its typical applications, namely, transport of photons in biological tissue for optical tomography (OT). In OT a laser beam illuminates the imaged sample through its boundary and an image is then produced from the diffuse reflected and/or transmitted light. It is well accepted that the scattering of

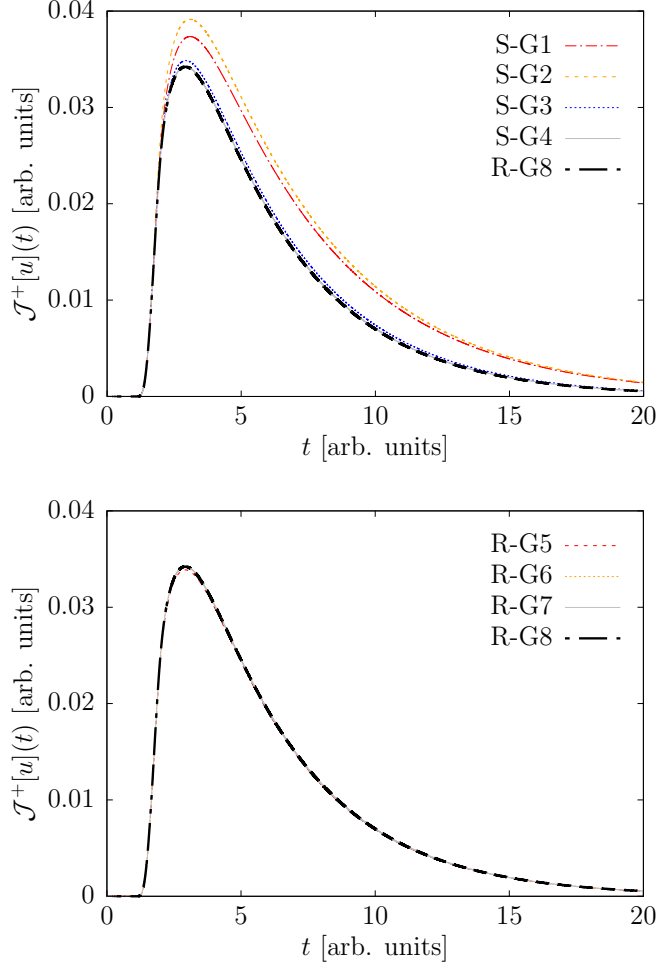


FIG. 4. Detector readings $\mathcal{J}^+(t)$ in arbitrary units (arb. units) for the S and R methods and for the various grids described in Table I; cf. Ref. [58, Fig. 7]. Top panel: S method curves for the grids G1–G4 compared to the reference R method curve for the fine grid G8 described in the text. Bottom panel: R method curves for the grids G5–G7 once again compared to the reference R-G8 curve, illustrating the significantly faster convergence of the R method.

photons by biological tissue is characterized by the combination of a scattering coefficient μ_s with values of up to hundreds per cm together with a 3D phase function (43) [and, thus, for the 1D cases considered in this paper, the phase version (45)] with anisotropy factors in the range $0.71 \leq g \leq 0.97$ [51,59]. For our test we thus consider the time-dependent RTE problem (3) with $g = 0.95$, $\mu_s = 100/\text{cm}$, $\mu_a = 0.01/\text{cm}$, $n_\Omega = 1.37$, and $n_s = 1$, with a source $\ell_0(\xi, t) = T(t)\delta(\xi - \xi_\ell)$ at $x = 0$ which, using a smooth Gaussian-like window function $T(t)$, models a laser pulse collimated in the direction $\xi = \xi_\ell$ incident on the left sample boundary, and without sources [$\ell_1(\xi, t) = 0$] imposed on the $x = 1$ boundary. (In the specific numerical test case presented below in the section the value $\xi_\ell = 1$, which corresponds to normal incidence, was used.)

Given the singular character of the collimated boundary source $\ell_0(\xi, t)$ considered here, this benchmark additionally provides guidelines on a possible implementation of the proposed algorithm in certain practical settings wherein the

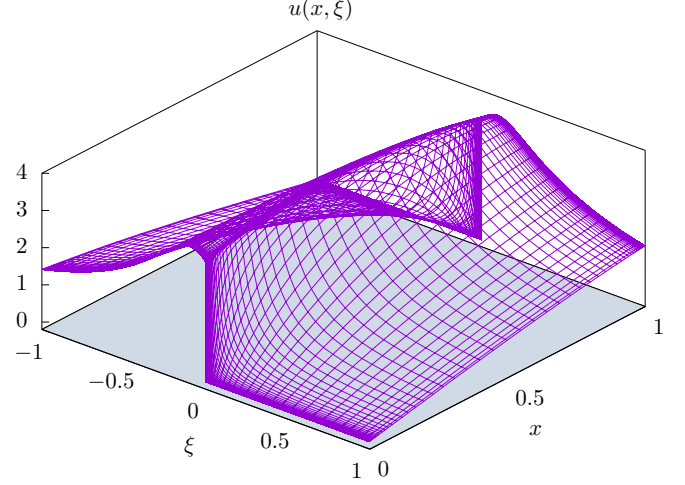


FIG. 5. Volumetric source boundary layer [$\ell_i(\xi) = 0$, $i = 0, 1$ and $\mathcal{R}^{0,1}(\xi) = 0$] for isotropic scattering media with $\mu_s = 0.5$, $\mu_a = 0.1$, $\mu_t = \mu_s + \mu_a = 1$, and $q = 1$, exhibiting the characteristic large slopes, with infinite slopes in the limits as $(x, \xi) \rightarrow (0^+, 0^+)$ and $(x, \xi) \rightarrow (1^-, 0^-)$.

assumption of smoothness of the boundary sources ℓ_j (introduced in Sec. III C) is not fulfilled. To efficiently treat such a collimated irradiation, the angular photon flux is expressed as the sum [60,61]

$$u(x, \xi, t) = u^1(x, \xi, t) + u^2(x, \xi, t) \quad (52)$$

of uncollided and diffuse fluxes denoted by $u^1(x, \xi, t)$ and $u^2(x, \xi, t)$, respectively. The uncollided flux, which contains the singularity of the solution, is taken to equal the solution of the equation

$$\left[\frac{1}{c} \frac{\partial}{\partial t} + \xi \frac{\partial}{\partial x} + \mu_t(x) \right] u^1(x, \xi, t) = 0,$$

$$u^1(x, \xi, t = 0) = 0,$$

$$u^1(0, \xi, t) = \mathcal{R}^0(\xi)u^1(0, \xi_R, t) + \ell_0(\xi, t), \quad \xi > 0,$$

$$u^1(1, \xi, t) = \mathcal{R}^1(\xi)u^1(1, \xi_R, t), \quad \xi < 0,$$

which can readily be obtained in closed form, given below, via application of the method of characteristics and consideration of multiple reflections. It follows that the diffuse flux satisfies the RTE

$$\left[\frac{1}{c} \frac{\partial}{\partial t} + \xi \frac{\partial}{\partial x} + \mu_t(x) \right] u^2(x, \xi, t)$$

$$= \mu_s(x) \int_{-1}^1 p(\xi, \xi') [u^2(x, \xi', t) + u^1(x, \xi', t)] d\xi',$$

$$u^2(x, \xi, t = 0) = 0,$$

$$u^2(0, \xi, t) = \mathcal{R}^0(\xi)u^2(0, \xi_R, t), \quad \xi > 0,$$

$$u^2(1, \xi, t) = \mathcal{R}^1(\xi)u^2(1, \xi_R, t), \quad \xi < 0, \quad (53)$$

whose solution can be obtained effectively by means of the linear-transport solver presented in this paper (Sec. IV).

The multiple reflections inherent in the solution $u^1(x, \xi, t)$ are accounted for in the closed form expression

$$u^1(x, \xi, t) = e^{-\int_0^x \frac{\mu_t(x')}{\xi} dx'} \delta(\xi - \xi_\ell) \sum_{n=0}^{\infty} \mathcal{R}^0(\xi)^{2n} \\ \times e^{-2n \int_0^1 \frac{\mu_t(x')}{\xi} dx'} T\left(t - \frac{2n}{c\xi} - \frac{x}{c\xi}\right), \quad \xi > 0, \\ u^1(x, \xi, t) = e^{-\int_1^x \frac{\mu_t(x')}{\xi} dx'} \delta(\xi - \xi_{\ell,R}) \\ \times \sum_{n=0}^{\infty} \mathcal{R}^1(\xi)^{2n+1} e^{(2n+1) \int_0^1 \frac{\mu_t(x')}{\xi} dx'} \\ \times T\left(t + \frac{2n+1}{c\xi} + \frac{1-x}{c\xi}\right), \quad \xi < 0.$$

The integral of the function $u^1(x, \xi, t)$ which appears in the RTE for u^2 can also be obtained in closed form:

$$\int_{-1}^1 p(\xi, \xi') u^1(x, \xi', t) d\xi' = p(\xi, \xi_\ell) e^{-\int_0^x \frac{\mu_t(x')}{\xi} dx'} \\ \times \sum_{n=0}^{\infty} \left[\mathcal{R}^0(\xi_\ell)^{2n} e^{-2n \int_0^1 \frac{\mu_t(x')}{\xi} dx'} T\left(t - \frac{2n}{c\xi_\ell} - \frac{x}{c\xi_\ell}\right) \right. \\ \left. + p(\xi, \xi_{\ell,R}) e^{-\int_1^x \frac{\mu_t(x')}{\xi_{\ell,R}} dx'} \mathcal{R}^1(\xi_{\ell,R})^{2n+1} \right. \\ \left. \times e^{(2n+1) \int_0^1 \frac{\mu_t(x')}{\xi_{\ell,R}} dx'} T\left(t + \frac{2n+1}{c\xi_{\ell,R}} + \frac{1-x}{c\xi_{\ell,R}}\right) \right].$$

Note that, for the large $\mu_t(x)$ values typically encountered in biological applications, only a few terms in this equation need to be retained. Further, as evidenced by this δ -function (collimated incident-beam) expression, the right-hand side of Eq. (53), and therefore the diffuse solution u^2 , inherit the sharp ξ slope around $\xi = \xi_\ell$ that is characteristic of the phase function p for the presently assumed high values of the anisotropy coefficient g . To numerically resolve the aforementioned sharp u^2 slope in the ξ variable around $\xi = \xi_\ell$ in addition to the incidence and Fresnel boundary-layer structures (see Sec. III A), we utilize a modified version of the change of variables (17)–(19)—which introduces graded meshes not only around $\xi = 0$ and $\xi = \xi_c^0$, but also around $\xi = \xi_\ell$. For the case $\xi_\ell = 1$ considered in this section, this can be achieved by introducing modified versions of the functions $s(r)$ and $\psi(r)$ in Eqs. (17) and (19). The new versions of these functions are obtained by redefining them in the region $\xi_c^0 < r \leq 1$ according to the expressions

$$s(r) = 2\pi \left(\frac{r - \xi_c^0}{1 - \xi_c^0} \right), \\ \psi(r) = \xi_c^0 + \frac{1 - \xi_c^0}{2\pi} h(s(r)). \quad (54)$$

Figure 4 and Table I demonstrate the benefits that ensue, even for the challenging high- g and collimated-illumination problem considered in this section, as a result of the proposed “resolution” method (referred to in this section as the R method), which incorporates (i) the introduction of the boundary-layer-resolving changes of variables (16) and (18)–(19) (for spatial and angular boundary layers, respectively,

TABLE I. Convergence of S and R methods.

	N	M	T	L	v_{\max}	t_c (s)	ε
S-G1	100	80	1×10^4	–	–	5.8	2.2×10^{-1}
S-G2	200	80	2×10^4	–	–	26.1	2.7×10^{-1}
S-G3	250	100	2×10^4	–	–	59.1	2.9×10^{-2}
S-G4	250	120	2×10^4	–	–	80.4	2.7×10^{-3}
R-G5	80	40	5×10^3	5	10	2.3	1.0×10^{-2}
R-G6	100	44	5×10^3	5	15	3.4	1.4×10^{-3}
R-G7	150	60	2×10^4	10	15	50.0	7.6×10^{-5}

see also point (iii) below); (ii) the phase-function resolving precomputation strategy embodied in Eqs. (48) and (49); as well as, (iii) the modified version (54) of the angular change of variables that additionally resolves the aforementioned sharp slope in the ξ variable around $\xi = \xi_\ell$. To appreciate these benefits we compare the results obtained by means of the R method to those produced by a “standard” implicit FC-based method, referred to in this paper as the S method, which utilizes equispaced spatiotemporal grids together with Gauss-Legendre angular integration on the entire interval $-1 \leq \xi \leq 1$, and without use of any of the resolving changes of variables (i) and (iii) or precomputation strategy (ii). Figure 4 thus compares the values of the detector readings $\mathcal{J}^+(t)$ [Eq. (8)] produced by the S and R methods. Clearly, as the grids are refined, the curves S-G1 to S-G4 (method S with grids G1 through G4; see Table I) eventually approach the accurate R-G8 curve $\mathcal{J}_f^+(t)$ (method R with a fine G8 described containing $N = 1080$ equispaced spatial discretization points in the interval $[v_{\min}, v_{\max}] = [-27, 27]$ and $T = 20\,000$ discretization points in the time interval $[0, 20]$ together with $M = 120$ angular quadrature points and a Legendre polynomial expansion as described in Sec. IV B of order $L = 20$). The lower panel in the figure demonstrates a much faster convergence for the R method as the grids are refined. Table I displays the relative L^2 error

$$\varepsilon = \sqrt{\frac{\int_0^{t_{\max}} |\mathcal{J}^+(t) - \mathcal{J}_f^+(t)|^2 dt}{\int_0^{t_{\max}} \mathcal{J}_f^+(t)^2 dt}},$$

corresponding to each one of the grids considered. Once again we see that the R method is advantageous even for the highly anisotropic and collimated-beam problem (anisotropy factor $g = 0.95$) considered. For instance, the S-G4 detector readings, which contain an error of 2.7×10^{-3} , required a computing time of 80.4 s, while a slightly better error (1.4×10^{-3}) was produced with R-G2 in only 3.4 s—approximately 24 times faster.

C. Illustration of boundary-layer structures and their analytic regularization

In practice, the proposed changes of variables in the ξ and x variables result in spatial and angular grids meshes that are graded toward the various boundary-layer structures identified, and thus produce the desired boundary-layer resolution. The geometry underlying the boundary-layer structures is demonstrated in Secs. VC 1 and VC 3; the graded grids that result from the changes of variables used can be appreciated in

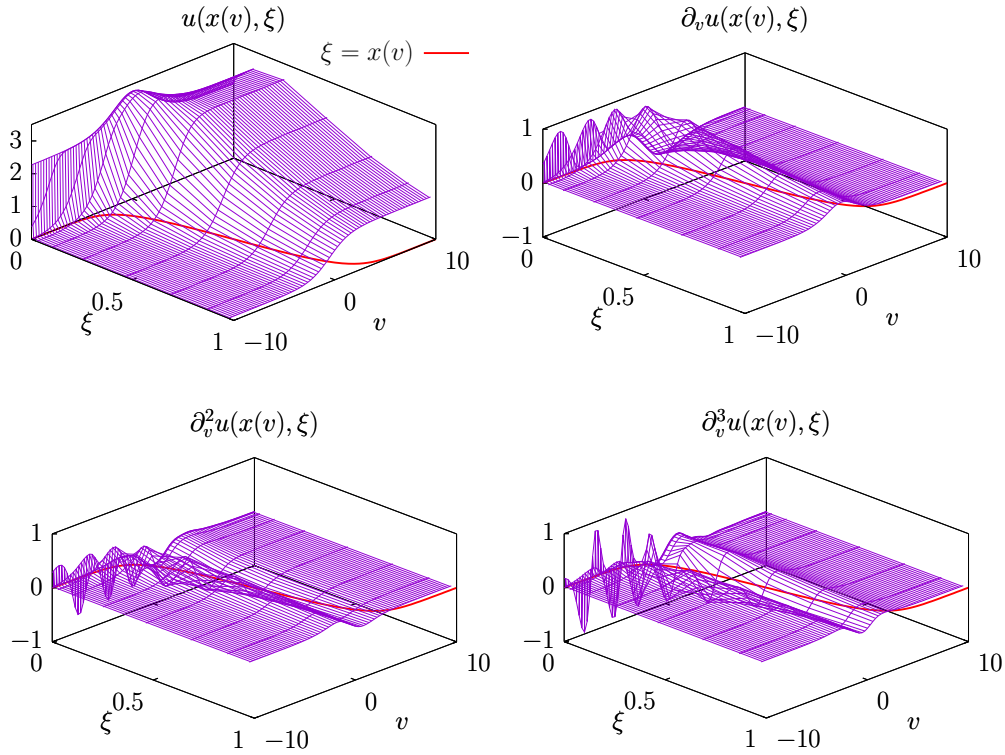


FIG. 6. From top to bottom and left to right: transport solution $u(x(v), \xi)$ and its first, second, and third derivatives with respect to the variable v . In this example we have set $\ell_i(\xi) = 0$, $i = 0, 1$ and $\mathcal{R}^{0,1}(\xi) = 0$, in anisotropic scattering media with $\mu_s = 0.95$, $\mu_a = 0.05$, $g = 0.8$, and $q = 1$. The red curve $\xi = x(v)$ delimits the boundary-layer region. Inside the boundary layer [$x(v) < \xi$] in the new v variable all derivatives become vanishingly small as $v \rightarrow -\infty$ for all finite values of ξ .

Figs. 5 and 7. The resolution effect is discussed in a particular example in Sec. VC2 and is illustrated in Fig. 6.

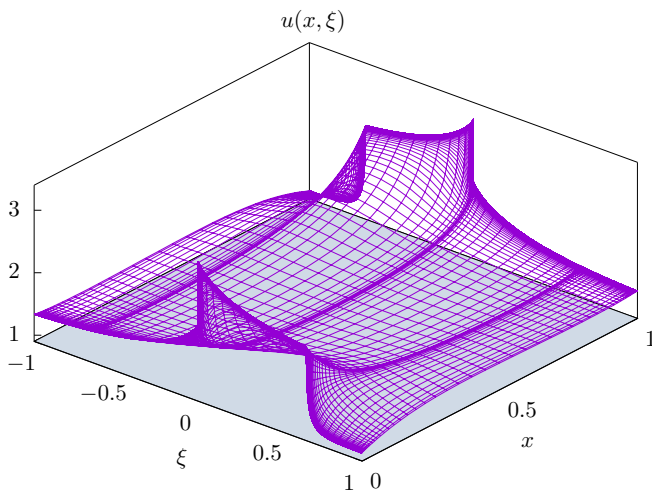


FIG. 7. Boundary layers under the presence of Fresnel and Incidence boundary conditions. In this problem two isotropic sources injecting radiation at $x = 0$ and $x = 1$ [$\ell_i(\xi) = 1$, $i = 0, 1$ in Eq. (1)] were considered, with $q = 0$, $\mu_a = 0.1$, $\mu_s = 9.9$, $g = 0.8$, $n_s = 1$, and $n_\Omega = 1.33$, giving $\xi_c^{0,1} \simeq \pm 0.6593$. Note the high slopes that now occur for $(x, \xi) \rightarrow (0^+, 0^+)$ and also for $(x, \xi) \rightarrow (0^+, \xi_c^0)$.

1. Volumetric source boundary layers

This section concerns applications for which the indices of refraction of the media and its surroundings coincide ($n_\Omega = n_s$), and for which there are no sources in the boundary of the domain Ω . In such cases, which arise often in applications wherein the neutral particles originate in the interior of the participating media, such as the transport of both photons produced by fluorescence as well as neutrons originating in nuclear fission reactions, vacuum boundary conditions ($u(x, \xi) = 0$ at $x = 0$ and $x = 1$ for all incoming directions) must be imposed. In such cases the first summand on the right-hand side of Eq. (10), which contains the boundary-conditions term ($\ell_0(\xi) + \mathcal{R}^0(\xi)u(0, \xi_R)$), vanishes, and only the volumetric terms remain—thus giving rise to the “volumetric source boundary layers” illustrated in Fig. 5. As can be appreciated in the figure, these boundary layers are characterized by large slopes in both the spatial and angular variables x and ξ near the boundary points $x = 0$ and $x = 1$ for values of the angular variable ξ close to $\xi = 0$ (with $\xi > 0$ for x near 0 and $\xi < 0$ for x near 1). Infinite slopes actually occur in the limits as $(x, \xi) \rightarrow (0^+, 0^+)$ and $(x, \xi) \rightarrow (1^-, 0^-)$.

2. Volumetric source boundary layer under spatial and angular changes of variables

The effect produced by the spatial change of variables (16) is demonstrated in Fig. 6 for a problem with vacuum boundary conditions. This figure thus displays the solution $u(x(v), \xi)$

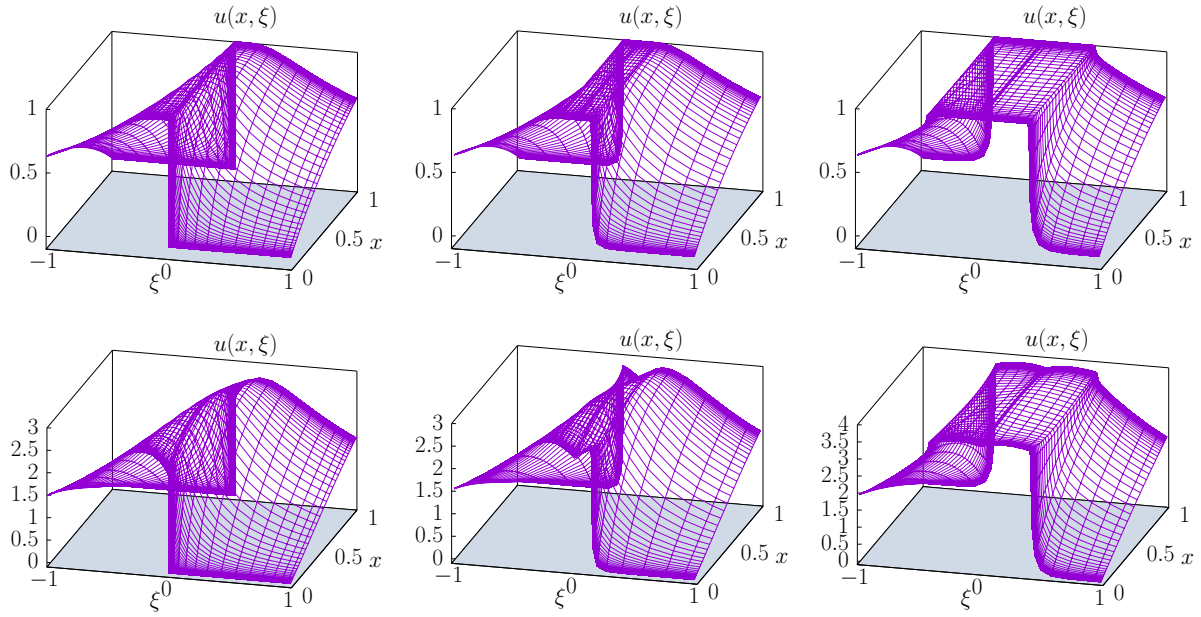


FIG. 8. Transport solution $u(x, \xi)$ exhibiting the boundary-layer structures for increasing values of n_Ω , starting from $n_\Omega = n_s$ (vacuum). The top panels display the analytic solution (D1) for problem parameters $\mu_s = 0, \mu_a = q = 1$. The bottom panels, in turn, display the numerical solution obtained for $\mu_s = q = 1, \mu_a = 0$, and $g = 0.5$. From left to right we have set: $n_\Omega = n_s = 1, n_\Omega = 1.01$, and $n_\Omega = 1.1$, respectively.

and its derivatives with respect to v variable in the region $\xi > 0$ [the values for $\xi < 0$ are not shown, since the solution u satisfies the symmetry relation $u(x, \xi) = u(1 - x, -\xi)$ for the problem considered here]. The red curve $\xi = x(v)$ delimits the boundary-layer region considered in the regularization proof presented in Sec. III D; see also Remark 2. Clearly, as established in Sec. III D, the v -derivatives of the transport solution are bounded throughout the spatioangular domain. A similar regularization effect is observed for the function $u(x, \Psi(r))d\Psi/dr$: derivatives of this function with respect to r are bounded up to order $(n - 1)$ [Eq. (25)]; an illustration of this regularization effect is omitted, for brevity.

3. Boundary-layer pairs under general Fresnel-Incidence boundary conditions

As discussed in Sec. III C, under Fresnel boundary conditions unbounded derivatives emerge in the limits as $(x, \xi) \rightarrow (0^+, \xi_c^0)$ and $(x, \xi) \rightarrow (1^-, \xi_c^1)$, where ξ_c^0 and ξ_c^1 denote the critical abscissas of total internal reflection defined in Eq. (6); the existence of such Fresnel boundary layers is illustrated in Fig. 7—which displays these boundary layers in addition to the $\xi = 0$ boundary layers of the type considered in Sec. V C 2 (Incidence boundary layers). As established in Sec. III C, the proposed changes of variables completely regularize the Fresnel boundary layers: as indicated in connection with Eq. (31), the r derivatives of the solution u with respect to r are bounded to all orders of differentiation.

4. Special case: Volume-source and Fresnel boundary-layer transition

In cases in which Fresnel boundary conditions are imposed (with index of refraction of the medium n_Ω exceeds that of the surroundings n_s , for which total internal reflection occurs) and in absence of boundary sources, the FBL takes on spatial

characteristics that differ from those studied previously in this paper. Under such scenarios, the Fresnel coefficient equals 1 in a neighborhood of $\xi = 0$ and, in the assumed absence of boundary sources $\ell_i(\xi)$, the Fresnel boundary conditions become, e.g., $u(0, \xi) = u(0, -\xi)$ for $\xi > 0$, and they therefore imply continuity of the angular flux u at $(x, \xi) = (0, 0)$ and $(x, \xi) \rightarrow (1, 0)$ —thereby eliminating the discontinuous boundary layers considered previously.

Such boundary-layer character may be illustrated by consideration of the transition that occurs as the index of refraction of the medium n_Ω is increased from an initial value $n_\Omega = n_s$ —which corresponds to vacuum boundary conditions under the present assumptions $\ell_i = 0$ —to a range of values $n_\Omega > n_s$, for which total internal reflection occurs. This section presents two such illustrations, namely: (i) in the case which an exact solution, Eq. (D1), may be obtained—with $\ell_i = 0, i = 1, 2$, in absence of scattering ($\mu_s = 0$), and with constant values of q and μ_a , with solutions depicted in the upper row of images in Fig. 8; and (ii) by consideration of numerical solutions including nonvanishing scattering, with the parameter values given in Fig. 8, and with solutions depicted on the lower row of images in the figure. Transitions from pure VSBL structures to FBL structure can be clearly appreciated in both of these rows of images, as the discontinuity at $x = 0$, which is present in the first image of each row, is clearly absent in all other images (cf. Fig. 7 where both a ISL and FSL coexist). However, the VSBL structure is not completely absent in the second row of images—which may be explained by consideration of the higher-order terms in the Neumann series (20), which contain the VSBL singularity albeit with diminished strength—on account of the fact that the higher-order Neumann series terms contain the VSBL in integrated form. For the exact solution in the first row of images in Fig. 7, all of the Neumann series terms of orders ≥ 1 vanish, and, thus, for $n_\Omega > n_s$ the VSBL (which in principle for the

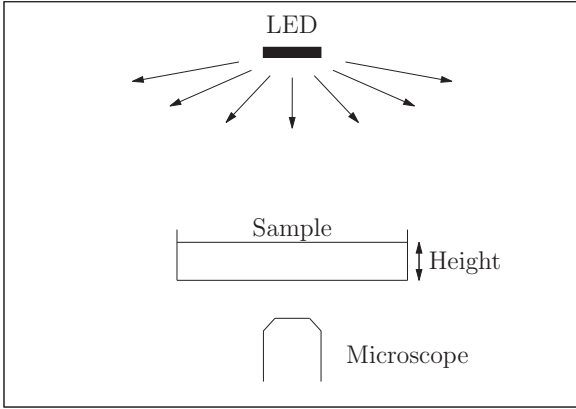


FIG. 9. Sketch illustrating the proof of concept experiment used to measure transmitted photons through a sample, which are subsequently collected by an optical microscope. In particular note the LED source, the sample height, and the microscope, in an overall photon transmission setup.

$q \neq 0$ value used would retain some degree of singularity) is completely eliminated.

D. Comparison of simulations and experiments

This section presents a comparison of computational results with experimental data for transmission of light across a turbid media. The experimental data used for our comparisons was obtained from a commercial confocal laser scanning microscope otherwise used in the context of fluorescence microscopy. In our proof of concept experiment, we substitute the fluorescence excitation light by a steady-state light emitting diode (LED) with a peak emission at 635 nm wavelength. Figure 9 presents the experimental setup. An LED injects radiation into a sample consisting of a mixture of distilled water and milk with varying milk concentrations and heights. Milk is a natural emulsion composed of fat particles dispersed in milk plasma. The plasma itself is a colloidal structure of proteins and minerals suspended in water. The protein molecules aggregate into small particles called micelles, typically ranging in size from 40 to 300 nm. Fat globules sizes, which are typically influenced by a variety of factors, range from 1 to 15 μm . All of these colloidal particles contribute significantly to light scattering, especially in visible and near-infrared.

The radiation emitted by the LED and transmitted through the sample is collected by the microscope as indicated in the figure. To compare experimental and simulated results, we employ the optical parameters reported in Ref. [62], for milk at the 680 nm light wavelength, and we thus use a diffraction grating and a bandpass filter to select the transmitted photons in the window between 660 and 700 nm that lie in the tail of the LED spectrum.

Further details on the instrumentation utilized and the propagation of uncertainties can be found in Appendix C. Figure 10, which displays the transmitted photon flux [Eq. (8)], demonstrates the ability of the proposed 1D numerical method to accurately reproduce the experimental observation of the intensity of photons collected by the microscope.

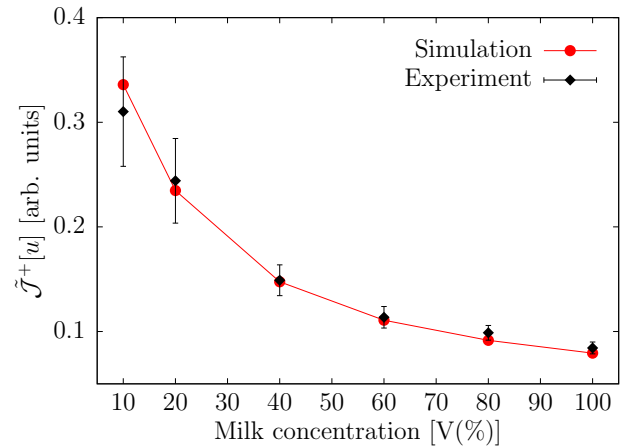
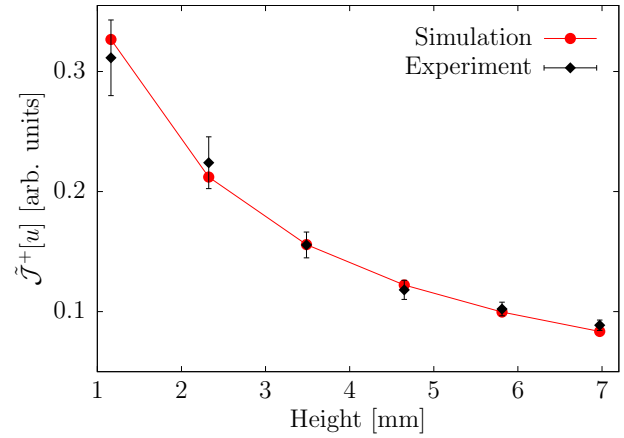


FIG. 10. Comparison of experimental and simulated normalized photon flux values $\tilde{\mathcal{J}}^+$ [Eqs. (8) and (C1)] for photons collected by a confocal microscope through samples containing either milk or an emulsion of milk in distilled water (3% fat milk was used in all cases). Top panel: results for samples of varying heights with whole milk. Bottom panel: data for samples made of emulsions of milk in distilled water at various concentrations. In all the experiments we maintained the sample height constant.

VI. CONCLUSIONS AND OUTLOOK

This work generalized and completed a 1D description of boundary layers that arise in linear transport theory, including associated theoretical analysis and construction of numerical solvers. Ongoing work seeks to generalize these ideas and methods to the full 3D context, in the spirit of the three-dimensional implicit-explicit FC-based computational fluid-dynamics algorithms presented in Ref. [46]. In particular, this paper proposed changes of variables that capture the underlying physics of the problem—such as the exponential Incidence and volume source boundary layers that occur at directions nearly parallel to the boundary, and the sharp gradients introduced by either boundary conditions of Fresnel type and by collimated boundary sources. Additionally, this paper proposed a precomputation-based integration strategy for the evaluation of the scattering integral which is capable of resolving highly anisotropic phase functions with high accuracy and low computational cost. The efficiency of the overall proposed algorithm was demonstrated through a series

of benchmarks and models that mimic typical applications of photon and neutral particle linear transport. In a realistic test case presented in Sec. VB, for example, the proposed approach was shown to produce simulated detector readings with engineering accuracy in a computing time that is 24 times faster than a similar algorithm which does not properly resolve the boundary-layer structures, and Sec. VD demonstrates excellent agreement between theory and experiment. Such accurate simulations of detector readings are crucial elements for the solution of inverse problems in optical and fluorescence tomography since, as is well known [21,63], numerical errors may destabilize associated inverse-problem reconstructions.

We submit that, in view of their high near-boundary accuracy, the methods developed in the present work can additionally be extended to assist confocal fluorescence microscopy (CFM) techniques—by using, as proposed in Ref. [34], a combination of CFM and fluorescence tomography methods to help bypass a fundamental limitation in the CFM methods concerning the imaging of deep tissues in high-scattering media. Indeed a combined inverse problem solver can be envisioned that incorporates not only the ballistic photons (which are exponentially attenuated after a few millimeters [60]; see also Refs. [64–72]) and associated interference phenomena that are crucial in the CFM setting but which are not captured by radiative transfer theory, as well as the scattered photons, which can be detected several centimeters away from the source. Following Ref. [34] we hypothesize that an effective imaging algorithm could thus result by exploiting such combined data and incorporating simultaneous forward photon transport solvers and accurate forward solvers for the ballistic propagation of light as described by Maxwell’s equations, in an overall effective transport and Maxwell inverse problem solver capable of deeper imaging than is possible for the CFM microscopy technique alone.

Although beyond the scope of this work, which has been aimed at the transport of neutral particles, the boundary layers analyzed here—inherent to the solutions of Boltzmann-type equations near boundaries—are also expected to emerge in more general and broader contexts. Examples include nonlinear transport theories relevant in several research areas, as well as multigroup neutron transport.

ACKNOWLEDGMENTS

This work was partially supported by the Agencia Nacional de Promoción Científica y Tecnológica (ANPCyT), Argentina, under Grant No. PICT 2020-02718, and by the University of Buenos Aires under Grant No. UBACyT 20020220100088BA to L.C.E. E.L.G. acknowledges receiving a scholarship from the National Research Council of Argentina (CONICET). L.C.E. is a member of CIC-CONICET. O.P.B. gratefully acknowledges support from contracts DMS-2109831 (NSF), HR00111720035 (DARPA), FA9550-21-1-0373 (AFOSR), and N00014-16-1-2808 (ONR).

APPENDIX A: NEUMANN EXPANSION, OPERATORS, AND IDENTITIES

This section reviews a well-known Neumann series formalism which is utilized as part of the theoretical analysis presented in this paper. For notational simplicity this discussion restricts attention to Eq. (1) with spatially constant values of the coefficients μ_a , μ_s , and q ; the generalization to the case of variable coefficients is straightforward.

The construction relies on a number of functions and operators, including the function

$$g(x, \xi) = \begin{cases} \ell_0(\xi)e^{-\mu_a x/\xi} & \xi > 0, \\ \ell_1(\xi)e^{-\mu_a(x-1)/\xi} & \xi < 0, \end{cases} \quad (\text{A1})$$

and the operators

$$L[f](x, \xi) = \begin{cases} \frac{e^{-\mu_a x/\xi}}{\xi} \int_0^x e^{\mu_a y/\xi} f(y, \xi) dy & \xi > 0, \\ \frac{e^{-\mu_a x/\xi}}{\xi} \int_1^x e^{\mu_a y/\xi} f(y, \xi) dy & \xi < 0, \end{cases} \quad (\text{A2})$$

$$G[f](x, \xi) = \begin{cases} \mathcal{R}^0(\xi)f(0, -\xi)e^{-\mu_a x/\xi} & \xi > 0, \\ \mathcal{R}^1(\xi)f(1, -\xi)e^{-\mu_a(x-1)/\xi} & \xi < 0, \end{cases} \quad (\text{A3})$$

and

$$S[f](x, \xi) = \int_{-1}^1 p(\xi, \xi')f(x, \xi')d\xi'. \quad (\text{A4})$$

Using these basic elements together with the integrating factor for the differential equation it is easy to check that the solution of Eq. (1) satisfies the integral equation

$$u(x, \xi) = G[u](x, \xi) + \mu_s L[S[u]](x, \xi) + g(x, \xi) + L[q](x, \xi), \quad 0 < |\xi| \leq 1, \quad (\text{A5})$$

or, equivalently,

$$(\mathbb{I} - K)[u](x, \xi) = g(x, \xi) + L[q](x, \xi), \quad (\text{A6})$$

where

$$K = G + \mu_s LS. \quad (\text{A7})$$

Inverting the left-hand operator in Eq. (A6) and using the geometric series for the resulting inverse operator, we obtain the convergent expansion [1,40]

$$u(x, \xi) = (\mathbb{I} - K)^{-1}[g + L[q]](x, \xi) = \sum_{m=0}^{\infty} K^m[g + L[q]](x, \xi), \quad (\text{A8})$$

or, in other words,

$$u(x, \xi) = \sum_{m=0}^{\infty} u^m(x, \xi), \tag{A9}$$

where

$$u^0(x, \xi) = g(x, \xi) + L[q](x, \xi), \quad m = 0, \tag{A10}$$

and

$$u^m(x, \xi) = K[u^{m-1}](x, \xi), \quad m \geq 1. \tag{A11}$$

The analysis presented in Secs. III C and III D relies on use of a number of identities whose derivation results from straightforward but somewhat tedious manipulations, which can be established by mathematical induction. In particular, Sec. III C, where the change of variables $\xi = \zeta_1(r) = r^n$ ($\xi > 0$) is employed, relies on use of the following identities, where $a_\ell, b_s, c_\ell,$ and d_s are real coefficients:

$$\frac{\partial^j}{\partial r^j} (r^{n-1} f(x, r^n)) = \sum_{\ell=0}^j a_\ell r^{(j+1-\ell)(n-1)-\ell} \frac{\partial^{j-\ell}}{\partial \xi^{j-\ell}} f(x, r^n), \tag{A12}$$

$$\frac{\partial^\alpha}{\partial \xi^\alpha} e^{-\mu_r x/\xi} = \frac{e^{-\mu_r x/\xi}}{\xi^{2\alpha}} \sum_{s=0}^{\alpha-1} b_s \xi^s (\mu_r x)^{\alpha-s}, \tag{A13}$$

$$\frac{\partial^j}{\partial r^j} \left(\frac{e^{-\mu_r(y-x)/r^n}}{r} \right) = \frac{1}{r^{j+1}} \sum_{\ell=1}^j c_\ell \left(\frac{\mu_r(y-x)}{r^n} \right)^\ell e^{-\mu_r(y-x)/r^n}, \tag{A14}$$

$$\frac{\partial^j}{\partial r^j} f(x, r^n) = r^{n-j} \sum_{s=0}^{j-1} d_s (r^n)^s \frac{\partial^{s+1}}{\partial \xi^{s+1}} f(x, r^n). \tag{A15}$$

Using Eqs. (A14) and (A15) we further obtain

$$\frac{\partial^j}{\partial r^j} \left(\int_0^x \frac{e^{-\mu_r(y-x)/r^n}}{r} v(y, r^n) dy \right) = \sum_{k=0}^j \binom{j}{k} r^{n-j-1} \int_0^x \sum_{s=1}^{j-k} d_s (r^n)^s \frac{\partial^s}{\partial \xi^s} v(y, r^n) \sum_{\ell=1}^j c_\ell \left(\frac{\mu_r(y-x)}{r^n} \right)^\ell e^{-\mu_r(y-x)/r^n} dy. \tag{A16}$$

Section III D, in turn, which utilizes the change of variables $x(v) = \frac{e^v}{e^v+1}$, relies on the identities (A17) through (A21) (where $a_\ell, b_{k,\ell}, c_{j,m,\alpha,\beta,\gamma,\delta}$ and $d_{j,k,w,\alpha,\beta,\delta,\gamma,s,\ell}$, denote real constants), all of which are valid for $j \geq 1$ and $\xi > 0$. In particular, use of simple differentiation rules yields the identities

$$\frac{\partial^j}{\partial v^j} x(v) = x(v) \sum_{\ell=0}^{j-1} a_\ell x(v)^\ell (x(v) - 1)^{j-\ell}, \tag{A17}$$

$$\frac{\partial^j}{\partial v^j} e^{-\mu_r x(v)/\xi} = e^{-\mu_r x(v)/\xi} \sum_{k=1}^j \left(\frac{\mu_r x(v)}{\xi} \right)^k \sum_{\ell=0}^k b_{k,\ell} x(v)^\ell. \tag{A18}$$

Integrating by parts k times in Eq. (A2), in turn, we obtain

$$L[f](x(v), \xi) = \sum_{\ell=1}^k (-1)^{\ell-1} \frac{\xi^{\ell-1}}{\mu_r^\ell} \left(\frac{\partial^{\ell-1}}{\partial x^{\ell-1}} f(x, \xi) - \frac{\partial^{\ell-1} f}{\partial x^{\ell-1}}(0, \xi) e^{-\mu_r x/\xi} \right) + (-1)^k e^{-\mu_r x/\xi} \frac{\xi^{k-1}}{\mu_r^k} \int_0^x e^{\mu_r y/\xi} \frac{\partial^k}{\partial y^k} f(y, \xi) dy. \tag{A19}$$

Combining Eqs. (A18) and (A19) and using Leibnitz' integral and product rules, further, the relation

$$\begin{aligned} \frac{\partial^j}{\partial v^j} L[f](x(v), \xi) &= \sum_{\ell=1}^k (-1)^{\ell-1} \frac{\xi^{\ell-1}}{\mu_r^\ell} \frac{\partial^j}{\partial v^j} \left(\frac{\partial^{\ell-1}}{\partial x^{\ell-1}} f(x(v), \xi) - e^{-\mu_r x(v)/\xi} \frac{\partial^{\ell-1} f}{\partial x^{\ell-1}}(0, \xi) \right) \\ &+ (-1)^k \frac{\xi^{k-1}}{\mu_r^k} \left[e^{-\mu_r x(v)/\xi} \sum_{m=1}^j \left(\frac{\mu_r x(v)}{\xi} \right)^m \sum_{\ell=0}^j b_{m,\ell} x(v)^\ell \int_0^{x(v)} e^{\mu_r y/\xi} \frac{\partial^k}{\partial y^k} f(y, \xi) dy \right. \\ &\left. + \sum_{m=1}^j \sum_{\alpha=1}^{j-m} \sum_{\beta=0}^{j-m-\alpha} \sum_{s=0}^{m-1-s} \sum_{\gamma=1}^{m-1-s} \sum_{\delta=0}^{j-m} c_{j,m,\alpha,\beta,\gamma,\delta} \left(\frac{\mu_r x(v)}{\xi} \right)^{\alpha+\gamma} x(v)^{\beta+\delta} \frac{\partial^s}{\partial v^s} \left(\frac{\partial^k}{\partial x^k} f(x(v), \xi) \frac{dx(v)}{dv} \right) \right] \tag{A20} \end{aligned}$$

results. In a variant of Eq. (A20), utilizing once again Leibnitz' rules in conjunction with the identities (A17) and (A18), but without use of integration by parts, we obtain

$$\begin{aligned} \frac{\partial^j}{\partial v^j} L[f](x(v), \xi) &= \sum_{k=1}^j \sum_{w,\alpha=1}^{j-k} \sum_{s=0}^{k-1} \sum_{\beta=0}^{k-s-1} \sum_{\ell=0}^s \sum_{\delta,\gamma=1}^{s-\ell} d_{j,k,w,\alpha,\beta,\delta,\gamma,s,\ell} \frac{1}{\mu_t} \left(\frac{\mu_t x(v)}{\xi} \right)^{\delta+w+1} (x(v)-1)^{k-s-\beta} x(v)^{\alpha+\beta+\gamma} \frac{\partial^\ell}{\partial v^\ell} f(x(v), \xi) \\ &+ \frac{e^{-\mu_t x/\xi}}{\xi} \int_0^{x(v)} e^{\mu_t y/\xi} f(y, \xi) dy \sum_{k=1}^j \left(\frac{\mu_t x(v)}{\xi} \right)^k \sum_{\ell=0}^j b_{k,\ell}. \end{aligned} \quad (\text{A21})$$

APPENDIX B: DERIVATIVE-BOUNDEDNESS FOR THE 1D HENYEV-GREENSTEIN PHASE FUNCTION

The analysis in Sec. III C and the fast convergence of the Legendre expansion of the phase function used in Sec. IV B both require the 1D phase function $p(\xi, \xi')$ to have bounded derivatives of various orders for all $-1 \leq \xi, \xi' \leq 1$. This section shows that this assumption does indeed hold true, to all nonnegative orders of differentiation, for the 1D version of the phase function considered most often for photon transport in the context of biological applications and used throughout this paper, namely, the 1D Henyey-Greenstein phase function. More precisely, in what follows we show that, for any given real anisotropy parameter $g \neq \pm 1$ ($|g| < 1$ in the biological-matter context of this paper), the 1D Henyey-Greenstein phase function (44) is an analytic function of both ξ' and ξ for $(\xi, \xi') \in [-1, 1] \times [-1, 1]$ —a condition that amply ensures the claimed derivative boundedness.

Using the relations $\xi = \cos(\theta)$, $\xi' = \cos(\theta')$ and

$$\hat{\omega}(\xi, \varphi) = \xi \hat{x} + \cos(\varphi) \sqrt{1 - \xi^2} \hat{y} + \sin(\varphi) \sqrt{1 - \xi^2} \hat{z},$$

and letting $\gamma = \hat{\omega}(\xi, \varphi) \times \hat{\omega}(\xi', \varphi')$ the scalar-product term in Eq. (B2), simple algebra gives

$$\begin{aligned} \gamma &= \hat{\omega}(\xi, \varphi) \times \hat{\omega}(\xi', \varphi') \\ &= \xi \xi' + \sqrt{1 - \xi^2} \sqrt{1 - \xi'^2} \cos(\varphi - \varphi'). \end{aligned} \quad (\text{B1})$$

In view of Eq. (44) the 1D HG phase function is given by integration of Eq. (43) with respect to φ' :

$$\begin{aligned} p(\xi, \xi') &= \int_0^{2\pi} \eta(\xi, \xi', \varphi - \varphi') d\varphi' \\ &= \frac{1}{4\pi} \int_0^{2\pi} \frac{1 - g^2}{(1 + g^2 - 2g\hat{\omega}(\xi, \varphi) \times \hat{\omega}(\xi', \varphi'))^{3/2}} d\varphi'. \end{aligned} \quad (\text{B2})$$

We note the square-root terms in Eq. (B1), whose derivatives with respect to ξ' (respectively, ξ) become unbounded as $\xi' \rightarrow 1$ (respectively, $\xi \rightarrow 1$)—in spite of which, as claimed above and shown in what follows, the 1D phase function (B2) has finite derivatives of all orders for $-1 \leq \xi, \xi' \leq 1$.

(Although convenient, the use made in this paper of the variables ξ and ξ' is not essential: the variables θ and θ' could be used instead, leading directly to finite phase-function

derivatives, even in the 3D case, as needed both in the analysis presented in Sec. III C and to achieve the fast convergence of a Legendre expansion of the phase function underlying the techniques presented in Sec. IV B.)

To establish the analyticity result for $(\xi, \xi') \in [-1, 1] \times [-1, 1]$, we let $\gamma_0 = \frac{1+g^2}{2g}$, we define

$$\tilde{\eta}(\gamma) = \frac{1 - g^2}{4\pi(1 + g^2 - 2g\gamma)^{3/2}} = C \frac{1}{(1 - \frac{\gamma}{\gamma_0})^{3/2}},$$

$$\text{where } C = \frac{1 - g^2}{4\pi(2g\gamma_0)^{3/2}},$$

and we use the Taylor series $(1 - \frac{\gamma}{\gamma_0})^{-3/2} = \sum_{j=0}^{\infty} b_j (\frac{\gamma}{\gamma_0})^j$, which we may express in the form

$$\eta = C \sum_{j=0}^{\infty} b_j \left[\frac{\xi \xi' + \sqrt{1 - \xi^2} \sqrt{1 - \xi'^2} \cos(\varphi - \varphi')}{\gamma_0} \right]^j. \quad (\text{B3})$$

Since $|\gamma| \leq 1$ for $(\xi, \xi') \in [-1, 1] \times [-1, 1]$, and since $|\gamma_0| = |\frac{1+g^2}{2g}| > 1$ (under the standing assumption $g \neq \pm 1$), we have $|\frac{\gamma}{\gamma_0}| < 1$, and, thus, the quantity in square brackets in Eq. (B3) is smaller than one in absolute value for $(\xi, \xi') \in [-1, 1] \times [-1, 1]$. It follows that the square-bracket quantity remains smaller than one for ξ and ξ' in a sufficiently small complex neighborhood $V \subset \mathbb{C}^2$, $[-1, 1] \times [-1, 1] \subset V$, of the 2D real domain $[-1, 1] \times [-1, 1]$ —wherein, on account of the square-root terms, the quantity in square brackets becomes multivalued as a function of ξ and ξ' . Clearly, it follows that the series (B3) converges uniformly for $(\xi, \xi', (\varphi - \varphi')) \in V \times \mathbb{R}$. Expanding each binomial term in Eq. (B3) we obtain the similarly uniformly convergent multivalued series

$$\begin{aligned} \eta(\xi, \xi', \varphi - \varphi') &= C \sum_{j=0}^{\infty} \frac{b_j}{\gamma_0^j} \sum_{k=0}^j \binom{j}{k} (\xi \xi')^{j-k} \\ &\quad \times (\sqrt{1 - \xi^2} \sqrt{1 - \xi'^2} \cos(\varphi - \varphi'))^k. \end{aligned} \quad (\text{B4})$$

Termwise integration of this uniformly convergent series with respect to φ' , in accordance with Eq. (B2), eliminates all multivalued (odd k) terms (since $\int_0^{2\pi} \cos(\varphi - \varphi')^k d\varphi' = 0$ for k odd). Further, as the even k powers cancel the square roots, the integrated version of Eq. (B4) presents $p(\xi, \xi')$ as a uniformly

convergent series of single-valued analytic functions defined in V . It follows that the 1D phase function $p(\xi, \xi')$ equals the sum of a uniformly convergent series of analytic functions of ξ and ξ' for $(\xi, \xi') \in V$, and thus, as it follows from an application of the Weierstrass complex-variables theorem on analyticity of uniform limits of analytic functions is itself an analytic function in this region, as needed.

APPENDIX C: DETAILS ON EXPERIMENTAL SETTING AND ERROR ESTIMATES

With reference to Sec. VD, experimental data was produced using a FLUOVIEW FV1000 confocal laser scanning microscope. Given the character of the 1D model used, the laser was turned off and an LED photon source was utilized instead in a transmission configuration, as illustrated in Fig. 9. An objective lens UPLSAPO of 10X and 0.40 numerical aperture was employed. The microscope was set on the XYT scan mode (scanning the sample's lower surface in Fig. 9) with sampling speed of 40.0 $\mu\text{s}/\text{Pixel}$, with pixel size set to 0.414 $\mu\text{m}/\text{Pixel}$, and with an image size of 52.578 $\mu\text{m} \times 52.578 \mu\text{m}$ —for a total 128 \times 128 pixels. The collimator aperture was set to 770 μm . To reduce statistical errors 100 consecutive images were collected for each sample and the experimental value of the photon flux $\mathcal{J}^+[u]$ for a given sample [Eq. (8)] was taken to equal the average of the 1 638 400 intensity values obtained for all pixels and all 100 images per sample. For comparison purposes, for both the experimental and simulated photon flux data [Eq. (8)], the *normalized* photon flux values

$$\tilde{\mathcal{J}}_i^+[u] = \frac{\mathcal{J}_i^+[u]}{\sum_j \mathcal{J}_j^+[u]} \quad (\text{C1})$$

were evaluated, and are displayed in Fig. 10. In Eq. (C1), for each of the datasets considered (various heights of pure milk, on the one hand, and various concentrations of the milk-water emulsion for a constant height, on the other hand) the index i denotes the various experimental and simulated data points obtained. Using measuring pipettes, milk, and water mixtures were prepared at various volume concentrations, and the heights of the samples (Fig. 9) were determined based on the volume of each sample. Considering the precision of the instrumentation used and accounting for appreciation errors due to surface tension effects, a volume error of $\delta V = 200 \text{ mm}^3$ was assumed.

Letting h , V_m , and V_w denote the height of the sample and the milk and water volumes, respectively, and calling $V = V_m + V_w$ and

$$V(\%) = 100 \times \left(\frac{V_m}{V} \right), \quad (\text{C2})$$

we obtain the relation

$$\delta \tilde{\mathcal{J}}_i^+(h, V(\%)) = \left| \frac{\partial \tilde{\mathcal{J}}_i^+}{\partial h} \right| \delta h + \left| \frac{\partial \tilde{\mathcal{J}}_i^+}{\partial V(\%)} \right| \delta V(\%) \quad (\text{C3})$$

for the error in the detector readings resulting from uncertainties in the sample height and concentration. Here, assuming the errors in determination of volumes of milk, water, and milk-water mixture all coincide, $\delta V_m = \delta V_w = \delta V$, we have set

$$\delta V(\%) = 100 \times \frac{\delta V}{V} \left(1 - \frac{V_m}{V} \right). \quad (\text{C4})$$

Since the sample was contained in a cylindrical recipient of radius r , finally, and since the δh error stemming from radius-measurement error were found to be orders of magnitude smaller than the error resulting from volume-measurement errors, the former errors were disregarded and the height error was thus estimated via the expression

$$\delta h \simeq \frac{\delta V}{\pi r^2}. \quad (\text{C5})$$

The two derivatives in Eq. (C3) were estimated on the basis of detector readings produced by the numerical solver for various heights and concentrations. The milk utilized in our samples is not exactly the same as the one used in the reference [62] from which we obtained values of the optical parameters μ_s and μ_a used in Sec. VD: 3% fat milk was utilized for the comparisons in that section, while reference [62] provides μ_s and μ_a parameter values for 3.5% fat milk. It was not possible to estimate the errors introduced by such differences in fat concentration. Although this might constitute a source of systematic error, the good agreement observed between experimental and simulated detector readings suggest that such discrepancies may possibly be safely disregarded.

APPENDIX D: SCATTERING-FREE ANALYTICAL SOLUTION

An analytical solution, which displays the boundary-layer phenomenology in the simple scattering-free case, can easily be obtained under the assumption of constant optical parameters and sources together with the scattering-free condition $\mu_s = 0$. In particular, Eq. (1) with constant parameters $\ell_i(\xi) = 0$, $\mu_t(x) = \mu_a(x) = \mu_a$, and $q(x, \xi) = q$, admits the analytical solution

$$u(x, \xi) = \begin{cases} \frac{q}{\mu_a} \left[1 - \frac{\eta^0(\xi)}{e^{\mu_a x / \xi}} \right] & \xi > 0, \\ \frac{q}{\mu_a} \left[1 - \frac{\eta^1(\xi)}{e^{\mu_a (x-1) / \xi}} \right] & \xi < 0, \end{cases} \quad (\text{D1})$$

where

$$\eta^{0,1}(\xi) = \frac{\mathcal{R}^{0,1}(|\xi|) - 1}{\mathcal{R}^{0,1}(|\xi|) e^{-\mu_a / |\xi|} - 1}.$$

[1] K. M. Case and P. F. Zweifel, *Linear Transport Theory*, 1st ed. (Addison-Wesley, Boston, MA, 1967).

[2] J. J. Duderstadt and W. R. Martin, *Transport theory*, 1st ed. (Wiley, New York, NY, 1979).

- [3] S. Chandrasekhar, *Radiative Transfer*, 1st ed. (Dover, London, UK, 1960).
- [4] A. Ishimaru, *Wave Propagation and Scattering in Random Media* (Academic Press, New York, NY, 1978), Vol. 2.
- [5] E. E. Lewis and W. F. Miller, *Computational Methods of Neutron Transport* (John Wiley and Sons, New York, NY, 1984).
- [6] A. G. Klein and S. A. Werner, Neutron optics, *Rep. Prog. Phys.* **46**, 259 (1983).
- [7] S. T. Thynell, Discrete-ordinates method in radiative heat transfer, *Int. J. Eng. Sci.* **36**, 1651 (1998).
- [8] J. R. Howell, M. P. Mengüç, and R. Siegel, *Thermal Radiation Heat Transfer*, 5th ed., edited by T. & F. Group (CRC Press, Boca Raton, FL, 2011).
- [9] J. Qin, J. J. Makela, F. Kamalabadi, and R. R. Meier, Radiative transfer modeling of the OI 135.6 nm emission in the nighttime ionosphere, *J. Geophys. Res., A: Space Phys.* **120**, 10116 (2015).
- [10] K. F. Dymond, S. E. Thonnard, R. P. McCoy, and R. J. Thomas, An optical remote sensing technique for determining nighttime F region electron density, *Radio Sci.* **32**, 1985 (1997).
- [11] Q. Zhu, S. H. Kurtzman, P. Hegde, S. Tannenbaum, M. Kane, M. Huang, N. G. Chen, B. Jagjivan, and K. Zarfos, Utilizing optical tomography with ultrasound localization to image heterogeneous hemoglobin distribution in large breast cancers, *Neoplasia* **7**, 263 (2005).
- [12] Q. Zhu, P. U. Hegde, A. Ricci, Jr., M. Kane, E. B. Cronin, Y. Ardeshirpour, C. Xu, A. Aguirre, S. H. Kurtzman, P. J. Deckers, and S. H. Tannenbaum, Early-stage invasive breast cancers: Potential role of optical tomography with US localization in assisting diagnosis, *Radiology* **256**, 367 (2010).
- [13] H. Fujii, Y. Yamada, K. Kobayashi, M. Watanabe, and Y. Hoshi, Modeling of light propagation in the human neck for diagnoses of thyroid cancers by diffuse optical tomography, *Int. J. Numer. Methods Biomed. Eng.* **33**, e2826 (2017).
- [14] O. N. Vassiliev, T. A. Wareing, J. McGhee, G. Failla, M. R. Salehpour, and F. Mourtada, Validation of a new grid-based Boltzmann equation solver for dose calculation in radiotherapy with photon beams, *Phys. Med. Biol.* **55**, 581 (2010).
- [15] A. D. Klose, U. Netz, J. Beuthan, and A. H. Hielscher, Optical tomography using the time-independent equation of radiative transfer—Part I: Forward model, *J. Quant. Spectrosc. Radiat. Transfer* **72**, 691 (2002).
- [16] U. Netz, J. Beuthan, and H. J. Cappius, Imaging of rheumatoid arthritis in finger joints, *Med. Laser Appl.* **16**, 306 (2001).
- [17] M. Schweiger and S. R. Arridge, Optical tomographic reconstruction in a complex head model using *a priori* region boundary information, *Phys. Med. Biol.* **44**, 2703 (1999).
- [18] D. Boas, D. Brooks, E. Miller, C. Dimarzio, M. Kilmer, R. Gaudette, and Q. Zhang, Imaging the body with diffuse optical tomography, *IEEE Signal Process. Mag.* **18**, 57 (2001).
- [19] A. H. Hielscher, A. D. Klose, and K. M. Hanson, Gradient-based iterative image reconstruction scheme for time-resolved optical tomography, *IEEE Trans. Med. Imaging* **18**, 262 (1999).
- [20] S. R. Arridge, Optical tomography in medical imaging, *Inverse Probl.* **15**, R41 (1999).
- [21] K. Ren, Recent developments in numerical techniques for transport-based medical imaging methods, *Commun. Comput. Phys.* **8**, 947 (2010).
- [22] E. W. Larsen, An overview of neutron transport problems and simulation techniques, in *Computational Methods in Transport*, edited by F. Graziani (Springer, Berlin, 2006), pp. 513–534.
- [23] R. Sanchez and N. J. McCormick, A review of neutron transport approximations, *Nucl. Sci. Eng.* **80**, 481 (1982).
- [24] F. Anli, F. Yaşa, S. Güngör, and H. Öztürk, T_N approximation to neutron transport equation and application to critical slab problem, *J. Quant. Spectrosc. Radiat. Transfer* **101**, 129 (2006).
- [25] E. G. Mishchenko and C. W. J. Beenakker, Radiative transfer theory for vacuum fluctuations, *Phys. Rev. Lett.* **83**, 5475 (1999).
- [26] R. Prasher, Generalized equation of phonon radiative transport, *Appl. Phys. Lett.* **83**, 48 (2003).
- [27] J. Przybilla, M. Korn, and U. Wegler, Radiative transfer of elastic waves versus finite difference simulations in two-dimensional random media, *J. Geophys. Res.: Solid Earth* **111**, 2005JB003952 (2006).
- [28] E. L. Gaggioli, D. M. Mitnik, and O. P. Bruno, Skin effect in neutron transport theory, *Phys. Rev. E* **104**, L032801 (2021).
- [29] E. W. Larsen and J. B. Keller, Asymptotic solution of neutron transport problems for small mean free paths, *J. Math. Phys.* **15**, 75 (1974).
- [30] E. W. Larsen, J. E. Morel, and W. F. Miller Jr, Asymptotic solutions of numerical transport problems in optically thick, diffusive regimes, *J. Comput. Phys.* **69**, 283 (1987).
- [31] T. Durduran, A. Yodh, B. Chance, and D. Boas, Does the photon-diffusion coefficient depend on absorption? *J. Opt. Soc. Am. A* **14**, 3358 (1997).
- [32] S. R. Arridge and J. C. Schotland, Optical tomography: Forward and inverse problems, *Inverse Probl.* **25**, 123010(2009).
- [33] T. Tarvainen and B. Cox, Quantitative photoacoustic tomography: Modeling and inverse problems, *J. Biomed. Opt.* **29**, S11509 (2024).
- [34] S. Gigan, Optical microscopy aims deep, *Nat. Photon.* **11**, 14 (2017).
- [35] M. Mishchenko, A. Lacis, and L. Travis, Errors induced by the neglect of polarization in radiance calculations for rayleigh-scattering atmospheres, *J. Quant. Spectrosc. Radiat. Transfer* **51**, 491 (1994).
- [36] S. P. Morgan and M. Ridgway, Polarization properties of light backscattered from a two layer scattering medium, *Opt. Express* **7**, 395 (2000).
- [37] R. Garcia, Fresnel boundary and interface conditions for polarized radiative transfer in a multilayer medium, *J. Quant. Spectrosc. Radiat. Transfer* **113**, 306 (2012).
- [38] C. M. Bender and S. A. Orszag, *Advanced Mathematical Methods for Scientists and Engineers I*, 1st ed. (Springer, Berlin, 1999).
- [39] D. Colton and R. Kress, *Inverse Acoustic and Electromagnetic Scattering Theory*, 4th ed. (Springer, New York, NY, 2019).
- [40] A. K. Jha, Y. Zhu, S. Arridge, D. F. Wong, and A. Rahmim, Incorporating reflection boundary conditions in the neumann series radiative transport equation: Application to photon propagation and reconstruction in diffuse optical imaging, *Biomed. Opt. Express* **9**, 1389 (2018).
- [41] L. N. Trefethen, Is Gauss quadrature better than Clenshaw–Curtis? *SIAM Rev.* **50**, 67 (2008).

- [42] R. Dautray and J. L. Lions, *Mathematical Analysis and Numerical Methods for Science and Technology* (Springer, Berlin, 1993), Vol. 6.
- [43] B. G. Petrović and A. Haghghat, Analysis of inherent oscillations in multidimensional S_N solutions of the neutron transport equation, *Nucl. Sci. Eng.* **124**, 31 (1996).
- [44] O. P. Bruno and M. Lyon, High-order unconditionally stable FC-AD solvers for general smooth domains I. Basic elements, *J. Comput. Phys.* **229**, 2009 (2010).
- [45] N. Albin and O. P. Bruno, A spectral FC solver for the compressible Navier–Stokes equations in general domains I: Explicit time-stepping, *J. Comput. Phys.* **230**, 6248 (2011).
- [46] O. P. Bruno, M. Cubillos, and E. Jimenez, Higher-order implicit-explicit multi-domain compressible Navier-Stokes solvers, *J. Comput. Phys.* **391**, 322 (2019).
- [47] E. L. Gaggioli, O. P. Bruno, and D. M. Mitnik, Light transport with the equation of radiative transfer: The Fourier continuation—Discrete ordinates (FC–DOM) method, *J. Quant. Spectrosc. Radiat. Transfer* **236**, 106589 (2019).
- [48] J. D. Lambert, *Numerical Methods for Ordinary Differential Systems: The Initial Value Problem* (John Wiley & Sons, New York, NY, 1991).
- [49] E. L. Gaggioli and O. P. Bruno, Parallel inverse-problem solver for time-domain optical tomography with perfect parallel scaling, *J. Quant. Spectrosc. Radiat. Transfer* **290**, 108300 (2022).
- [50] S. Sharma and S. Banerjee, Role of approximate phase functions in Monte Carlo simulation of light propagation in tissues, *J. Opt. A: Pure Appl. Opt.* **5**, 294 (2003).
- [51] A. N. Bashkatov, E. A. Genina, and V. V. Tuchin, Optical properties of skin, subcutaneous, and muscle tissues: A review, *J. Innovat. Opt. Health Sci.* **4**, 9 (2011).
- [52] W. Cheong, S. Prah, and A. Welch, A review of the optical properties of biological tissues, *IEEE J. Quantum Electron.* **26**, 2166 (1990).
- [53] M. Dehaes, L. Gagnon, F. Lesage, M. Péligrini-Issac, A. Vignaud, R. Valabregue, R. Grebe, F. Wallois, and H. Benali, Quantitative investigation of the effect of the extra-cerebral vasculature in diffuse optical imaging: A simulation study, *Biomed. Opt. Express* **2**, 680 (2011).
- [54] I. Gradshteyn and I. Ryzhik, *Table of Integrals, Series, and Products*, 7th ed. (Academic Press, San Diego, CA, 2007).
- [55] N. N. Lebedev, R. A. Silverman, and D. Livhtenberg, *Special Functions and Their Applications* (Dover Publications, Mineola, NY, 1965).
- [56] J. C. Chai, H. S. Lee, and S. V. Patankar, Ray effect and false scattering in the discrete ordinates method, *Numer. Heat Transfer B: Fund.* **24**, 373 (1993).
- [57] B. Hunter and Z. Guo, Conservation of asymmetry factor in phase function discretization for radiative transfer analysis in anisotropic scattering media, *Int. J. Heat Mass Transf.* **55**, 1544 (2012).
- [58] P. Granate, P. J. Coelho, and M. Roger, Radiative heat transfer in strongly forward scattering media using the discrete ordinates method, *J. Quant. Spectrosc. Radiat. Transfer* **172**, 110 (2016).
- [59] D. Fukutomi, K. Ishii, and K. Awazu, Determination of the scattering coefficient of biological tissue considering the wavelength and absorption dependence of the anisotropy factor, *Opt. Rev.* **23**, 291 (2016).
- [60] J. C. J. Paasschens, Solution of the time-dependent Boltzmann equation, *Phys. Rev. E* **56**, 1135 (1997).
- [61] M. F. Modest, *Radiative Heat Transfer*, 3rd ed. (Elsevier, New York, NY, 2013).
- [62] H. Wabnitz and H. Rinneberg, Imaging in turbid media by photon density waves: Spatial resolution and scaling relations, *Appl. Opt.* **36**, 64 (1997).
- [63] G. Bal, Inverse transport theory and applications, *Inverse Probl.* **25**, 053001 (2009).
- [64] A. Leray, C. Odin, E. Huguet, F. Amblard, and Y. L. Grand, Spatially distributed two-photon excitation fluorescence in scattering media: Experiments and time-resolved Monte Carlo simulations, *Opt. Commun.* **272**, 269 (2007).
- [65] F. Helmchen and W. Denk, Deep tissue two-photon microscopy, *Nat. Methods* **2**, 932 (2005).
- [66] E. A. Sergeeva, Scattering effect on the imaging depth limit in two-photon fluorescence microscopy, *Quantum Electron.* **40**, 411 (2010).
- [67] E. A. Sergeeva, A. R. Katichev, and M. Y. Kirillin, Two-photon fluorescence microscopy signal formation in highly scattering media: Theoretical and numerical simulation, *Quantum Electron.* **40**, 1053 (2011).
- [68] C. Berlage, M. L. S. Tantirigama, M. Babot, D. D. Battista, C. Whitmire, I. N. Papadopoulos, J. F. A. Poulet, M. Larkum, and B. Judkewitz, Deep tissue scattering compensation with three-photon F-SHARP, *Optica* **8**, 1613 (2021).
- [69] I. I. Fiks, M. Y. Kirillin, E. A. Sergeeva, and I. V. Tuchin, Reconstruction of object location for diffuse fluorescence tomography on the basis of hybrid models of light scattering in biotissues, *Radiophys. Quantum Electron.* **54**, 197 (2011).
- [70] B. Judkewitz, Y. M. Wang, R. Horstmeyer, A. Mathy, and C. Yang, Speckle-scale focusing in the diffusive regime with time reversal of variance-encoded light (TROVE), *Nat. Photon.* **7**, 300 (2013).
- [71] A. Dvornikov and E. Gratton, Imaging in turbid media: A transmission detector gives 2-3 order of magnitude enhanced sensitivity compared to EPI detection schemes, *Biomed. Opt. Express* **7**, 3747 (2016).
- [72] I. N. Papadopoulos, J. S. Jouhanneau, N. Takahashi, D. Kaplan, M. Larkum, J. Poulet, and B. Judkewitz, Dynamic conjugate F-SHARP microscopy, *Light: Sci. Appl.* **9**, 110 (2020).